

LIPS III: The Large Interstellar Polarisation Survey

Observational constraints on grain structures and alignment efficiencies

Ralf Siebenmorgen¹, Stefano Bagnulo², Thomas Vannieuwenhuyse¹, Lapo Fanciullo³, Vincent Guillet^{4,5}

¹ European Southern Observatory, Karl-Schwarzschild-Str. 2, 85748 Garching, Germany email: Ralf.Siebenmorgen@eso.org

² Armagh Observatory and Planetarium, College Hill, Armagh BT61 9DG, UK

³ National Chung Hsing University, 145 Xingda Rd., South Dist., Taichung City 402, Taiwan

⁴ Institut d'Astrophysique Spatiale, CNRS, Univ. Paris-Sud, Université Paris-Saclay, Bât. 121, 91405 Orsay cedex, France

⁵ Laboratoire Univers et Particules de Montpellier, Université de Montpellier, CNRS/IN2P2, CC 72, Place Eugène Bataillon, 34095 Montpellier Cedex 5, France

Received: June 6, 2025/ Accepted: XX X, 202X

ABSTRACT

The physical nature of dust in the diffuse interstellar medium remains incompletely understood, particularly with regard to the structure, composition, size distribution, and alignment properties of dust grains. Joint observations of reddening, starlight polarisation spectra, and polarized dust emission for individual sightlines provide essential constraints on these grain properties. This study focuses on modeling complementary observations of a far-UV-selected sample of 96 reddening curves along individual sightlines, for which optical linear polarisation spectra were obtained with FORS at the VLT as part of the Large Interstellar Polarisation Survey (LIPS). Spectra for 60 stars are presented in this work. These data are combined with Gaia distance estimates and thermal dust emission measurements from Planck. A three-component model, consisting of nanoparticles, amorphous grains, and submicrometre-sized grains, is employed. The axial ratios, porosities, sizes, element abundances, and alignment efficiencies of prolate-shaped particles are varied and compared to the observations using a multi-component fitting approach, which is made publicly available. The diversity of reddening and polarisation spectra among diffuse ISM sightlines is successfully reproduced using prolate-shaped grains with typical axial ratios of 2.5, porosity of 10%, and high alignment efficiency for dust particles larger than approximately $0.1\ \mu\text{m}$. However, the model parameters show significant variation from cloud to cloud, reflecting intrinsic differences in dust properties and local physical conditions. The results support the inclusion of submicrometre-sized grains, which contribute grey extinction in the optical, account for about one-third of the visual extinction, and carry roughly half of the dust mass. A follow-up submillimetre survey using a high spatial resolution polarimeter is required to refine the modeling of particle shapes and the alignment physics of large grains.

Key words. (ISM) dust, extinction

1. Introduction

Dust is ubiquitous in the interstellar medium (ISM). It plays a significant role in many astrophysical processes. In this article observational constraints are correlated with the physical properties of interstellar dust. A dust model is confronted against representative element depletion and stellar distance estimates, and characteristics of the reddening and polarisation—both in absorption and, where available, in emission—along individual sightlines through the diffuse ISM. For this purpose the Large Interstellar Polarisation Survey (LIPS) was performed to measure the starlight polarisation spectra of 161 stars using the FORS instrument (Appenzeller et al. 1998) on the ESO Very Large Telescope. The observations covered a wavelength range of $0.38 - 0.95\ \mu\text{m}$ at a spectral resolving power of ~ 880 . In LIPS I (Bagnulo et al. 2017), a catalog of 127 linear polarisation spectra corresponding to 101 sightlines was published.

Observing sightlines that intersect different components of the ISM introduces complexities in relating extinction and polarisation data to physical dust parameters. To address this issue, in LIPS II (Siebenmorgen et al. 2018), stars were observed with the high-resolution spectrograph UVES, which offers a resolving power of $\lambda/\Delta\lambda \sim 75,000$ (Dekker et al. 2000; Smoker et al. 2009). These spectra were used to confirm the spectral

type and luminosity class of the stars used for the reddening curve determination and to examine the profiles of interstellar absorption lines, particularly K_I. The concept of "single-cloud sightlines" was introduced, referring to cases where a dominant Doppler component accounts for more than half of the observed column density. A total of 65 such rare single-cloud sightlines were identified. It was found that interstellar polarisation is lower for multiple-cloud sightlines compared to single-cloud sightlines, indicating that the presence of additional clouds depolarises the transmitted radiation. Furthermore, significant variations in dust properties between different clouds were inferred from dust modeling.

In this work (LIPS III), the sample is expanded with additional FORS polarisation spectra for 60 stars. The same observing strategy, data reduction, and calibration procedures as detailed in LIPS I (Bagnulo et al. 2017) are applied. The importance of combining reddening and polarisation continuum observations is to constrain the nature of interstellar dust, including its chemical composition and size distribution. For instance, the reddening rise in the far-UV is indicative of very small nanoparticles, and so is the 2175\AA "bump" (e.g., Stecher & Donn 1965; Blasberger et al. 2017) which is tied to carbonaceous nanoparticles. The shape of the polarisation curve in the optical (Serkowski et al. 1975) can be used to constrain the size

distribution of aligned (large) dust grains (Kim & Martin 1995; Vaillancourt et al. 2020).

The reddening curves have been derived in the near-infrared (*JHK*) using the Two Micron All Sky Survey (2MASS) (Cutri et al. 2003), in the optical (*UBV*) from ground-based facilities (Valencic et al. 2004), and in the (far) ultraviolet (UV) below $0.3\,\mu\text{m}$ down to the Lyman limit from space-based observations. At these short wavelengths, the International Ultraviolet Explorer (IUE) and the Far Ultraviolet Spectroscopic Explorer (FUSE) observed spectra for 417 stars (Valencic et al. 2004), 328 stars (Fitzpatrick & Massa 2007), and 75 stars with FUSE (Gordon et al. 2009). Furthermore, distances derived from Gaia parallaxes were used to estimate the reddening at infinite wavelength providing an estimate of the visual extinction A_V .

The LIPS sample is further complemented by observations of polarised dust emission obtained from the Planck observatory at $850\,\mu\text{m}$ (Planck Collaboration et al. 2020). The Planck polarisation data is derived following the procedure outlined by Guillet et al. (2018).

2. The sample and data

The available $0.09\text{--}2.3\,\mu\text{m}$ reddening curves, complemented by UVES spectroscopy, Planck $850\,\mu\text{m}$ (353 GHz) polarimetry, and $0.38\text{--}0.92\,\mu\text{m}$ FORS spectropolarimetry, constitute the sample under investigation. It includes 96 stars, comprising 36 FORS polarisation spectra previously published in LIPS I and LIPS II, and 60 FORS polarisation spectra presented here. The characteristics of the sample are summarised in Table A.1, which lists the following 17 columns: For each star (col. 1), we specify the absolute Galactic latitude $|b|$ (col. 2). The Planck results are presented in four columns: surface brightness (I_{850} in MJy/sr) in col. 3, fractional polarisation (p_{850} in %) in col. 4, the polarisation angle in equatorial coordinates (θ_{850} in $^\circ$) in col. 5, and an estimate of the visual extinction A_V^{850} (col. 6), which is based on the Planck map of the dust optical depth at $850\,\mu\text{m}$ (Planck Collaboration et al. 2015).

The visual extinction A_V as determined from the GAIA parallax π (col. 7), and the reference extinction A_V^{ref} (col. 8) are provided. The latter is estimated by extrapolating optical/near-IR reddening to infinite wavelength, as given in the reddening curve catalogs by Valencic et al. (2004) (labelled V), Fitzpatrick & Massa (2007) (labelled F), and Gordon et al. (2009) (labelled G) in col. 9. We classify 55 single-cloud sightlines as 'S' and 41 multi-cloud sightlines as 'M' (col. 10).

The results of the FORS spectropolarimetry are summarized across seven columns. Observing dates are listed in col. 11. For stars observed multiple times, the final polarisation spectra are derived by averaging the Stokes parameters from individual observations. The fractional polarisation (p_V) and polarisation angle in equatorial coordinates (θ_V) at $0.55\,\mu\text{m}$ are provided in cols. 12 - 13. The gradient in the polarisation angle along the spectrum, $d\theta/d\lambda$ ($^\circ/\mu\text{m}$) is given in col. 14. In the optical, the observed interstellar polarisation spectra can be well approximated by a mathematical expression known as Serkowski (1973) formulae:

$$\frac{p(\lambda)}{p_{\text{max}}} = \exp \left[-k_p \ln^2 \left(\frac{\lambda_{\text{max}}}{\lambda} \right) \right], \quad (1)$$

The Serkowski parameters (p_{max} , λ_{max} , and k_p) derived from spectral fits to the FORS polarisation spectra are provided in cols. 15–17. The Serkowski fits for 43 stars, for which the available data do not permit detailed dust modeling, are shown in

Fig. 1. The spectral variation of the FORS polarisation angle, corrected for the optical reference value ($\theta - \theta_V$) is shown in Fig. 2.

In the LIPS sample, 27 stars are included in the stellar polarisation catalog by Heiles (2000), who detect 19 of these stars with high confidence at $p \gtrsim 0.6\%$. For these 19 stars, the linear polarisation agree in both catalogues, at $p = 0.14 \pm 0.08\%$, with larger deviations observed for HD 167264, HD 167771, and HD 168941. The polarisation angles are consistent within 3° , except for HD 092044, where the polarisation angles differ by 18° .

3. Dust model

We apply the dust model by Siebenmorgen (2023), which is consistent with current observational constraints on dust in the diffuse ISM (Hensley & Draine 2021). The model adopts representative solid-phase elemental abundances along the sightlines and successfully reproduces the observed wavelength-dependent reddening, emission, and polarisation from interstellar dust, spanning from the UV to microwave wavelengths. Furthermore, the model includes grey extinction by submicronmetre grains that reduce the luminosity distance, enabling consistency with trigonometric distances derived from Gaia parallaxes.

The number densities of the grains follow a power-law size distribution, $n(r) \propto r^{-q}$, with the same exponent q for each of the three dust populations: 1) Nanoparticles ($r \lesssim 6\text{ nm}$), including very small silicate (vSi), graphite (vgr), and polycyclic aromatic hydrocarbon (PAH). 2) Amorphous silicate (aSi) and carbon (aC) grains with sizes ranging between $6\text{ nm} \lesssim r \lesssim r_{\text{aSi}}^+ = r_{\text{aC}}^+ = 250\text{ nm}$. These are considered to have prolate rather than oblate shapes, as the former provide a better fit to observed linear polarisation spectra (Siebenmorgen et al. 2014). The grain radius is defined as that of a sphere whose volume is equal to that of the prolate particle, i.e., $r^3 = ab^2$, where a is the major axis and b is the minor axis. The mean grain radius of the amorphous grains, averaged over the size distribution, is typically $\bar{r}_{\text{aC,aSi}} \sim 30\text{ nm}$. 3) Submicrometre-sized dust aggregates ($250\text{ nm} \lesssim r < 3\,\mu\text{m}$) are treated as porous composites of component 2. The mean radius of these submicrometre-sized prolate shaped grains remains below $\bar{r}_\mu \lesssim 1\,\mu\text{m}$.

In the ISM, a grey component of micrometre-sized grains was introduced by Mathis et al. (1977) and by Wang et al. (2015a,b) to account for the observed infrared extinction. Such grains have also been incorporated into other dust models (Voshchinnikov 2004; Krügel & Siebenmorgen 1994; Krügel 2008; Ormel et al. 2011; Ysard et al. 2024). Recently, the impact of grey extinction on Type Ia supernova distance measurements was analyzed by the Dark Energy Survey Collaboration (Popovic et al. 2024). The submillimetre excess continuum emission in the Milky Way detected by Planck (Planck Collaboration et al. 2020) can be matched by adjusting the grain emissivity at these wavelengths (Hensley & Draine 2021). However, such models fail to resolve the discrepancy between trigonometric distance estimates provided by the Gaia Collaboration et al. (2023) and the overprediction of the luminosity distance of the same stars. Unification between luminosity and trigonometric distance estimates could be established by considering a population of submicrometre-sized dust (Siebenmorgen et al. 2025), which provides the necessary additional dimming of starlight. These grains are large enough to produce consistent reddening and grey extinction at wavelengths shorter than $1\,\mu\text{m}$.

The submicrometre-sized grains absorb a fraction of the interstellar radiation field (ISRF, Mathis et al. (1983); Bianchi (2024)). Because they are large, they remain cold and emit at

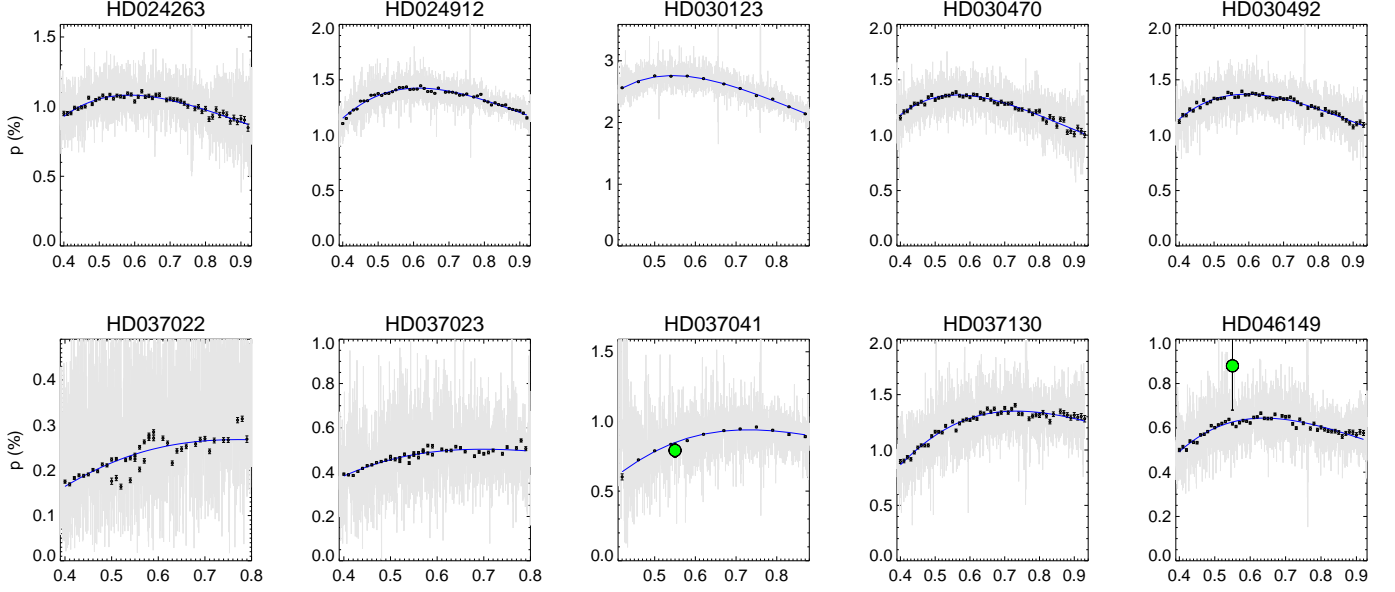


Fig. 1. FORS polarisation spectra of 43 stars. The grey lines show the original data, while the black open circles (with 1σ errors bars) represent the data rebinned at spectral resolution $\lambda/\Delta\lambda \sim 50$. The green circles represent the measurements available in the catalogue by Heiles (2000). The blue lines show the best-fits obtained with the Serkowski's formula. Continued in Figs. A.1 - A.2.

long wavelengths. Initially, very cold (10 K) dust emission was detected in our Galaxy toward high-density regions (Chini et al. 1993) and in non-active galaxies (Chini et al. 1995). This cold dust was later confirmed by ISO (Krügel et al. 1998; Siebenmorgen et al. 1999). More recently, excess emission at 0.5 mm observed by Herschel could not be explained by a single modified blackbody temperature component (Madden et al. 2013; Kennicutt et al. 2011; Rémy-Ruyer et al. 2013), with similar results confirmed using ALMA (Galliano et al. 2005) and LABOCA (Galamez et al. 2009) at even longer wavelengths. Furthermore, micrometre-sized particles from the diffuse ISM were directly measured in situ by the Ulysses, Galileo, and Stardust space probes (Landgraf et al. 2000; Westphal et al. 2014; Krüger et al. 2015). They appear in sightlines associated with the cold ISM (Siebenmorgen et al. 2020).

The cross-section $K_i(\lambda)$ ($\text{cm}^2/\text{g-dust}$) for the dust population i is given by

$$K_i(\lambda) = \frac{3}{4\pi} \frac{m_i}{\rho_i} \frac{\int_{r_i^-}^{r_i^+} C_i(r, \lambda) r^{-q} dr}{\int_{r_i^-}^{r_i^+} r^{3-q} dr}. \quad (2)$$

Optical constants are adopted from Zubko et al. (1996) for amorphous carbon, Draine (2003); Draine & Hensley (2021) for graphite and astro-silicate, and Demyk et al. (2022) for amorphous silicates, assuming a 97:3 mix in mass of $\text{MgO}-0.5 \text{ SiO}_2$ and $\text{Mg}_{0.8}\text{Fe}_{0.2}^{2+} \text{ SiO}_3$. The optical constant of porous and composite grains with vacuum inclusions are computed using the Bruggemann mixing rule. The molecular weights are $\mu_C = 12$ for carbon materials, $\mu_{\text{Si}} = 135$ for astro-silicate, and $\mu_{\text{aSi}} = 100$ for amorphous silicates. The bulk densities (g/cm^3) are for nanograins $\rho_{\text{vgr}} = 2.2$, $\rho_{\text{vSi}} = 3.5$, carbon particles $\rho_{\text{aC}} = 1.6$, amorphous silicates $\rho_{\text{aSi}} = 2.7$, and in submicrometre-sized grains $\rho_{\mu\text{Si}} = 3.4$.

The total extinction cross section, $K(\lambda)$, is the sum of K_i from all components¹. The cross sections, C , for absorption, scattering, and polarisation are provided in Eqs. 9 – 10. The relative mass of component i in 1 g of dust is:

$$m_i = \mu_i \frac{[X_i]}{[H]} \bigg/ \sum_i \mu_i \frac{[X_i]}{[H]}. \quad (3)$$

The elemental abundance in the dust relative to hydrogen in the gas phase $[X_i]/[H]$ is constrained to respect the depletion limits (Hensley & Draine 2021; Siebenmorgen 2023) so that

$$\frac{[C]}{[Si]} < 5.2. \quad (4)$$

The optical depth $\tau_V = A_V/1.086$ is

$$\tau_V = N^{na} K_V^{na} + N^{s\mu} K_V^{s\mu}, \quad (5)$$

where N^{na} represents the sum of the dust column density of nanoparticles and amorphous particles, while $N^{s\mu}$ is the dust column density of submicrometre-sized grains. The corresponding mass extinction cross-sections are denoted by K_V^{na} and $K_V^{s\mu}$, respectively. At infinite wavelengths, $K(\infty) = 0$, so that $A_V = -E(\infty - V) > -E(H - V)$ in the H -band. The reddening $E(B - V) = 1.086 (\tau_B - \tau_V)$ is

$$E(B - V) = N^{na} (K_B^{na} - K_V^{na}) + N^{s\mu} (K_B^{s\mu} - K_V^{s\mu}), \quad (6)$$

which provides a second constraint for estimating the relative mass fraction of the submicrometre-sized grains, $m_{s\mu} = N^{s\mu}/(N^{na} + N^{s\mu})$. This allows us to derive the absolute reddening of the model

¹ A suffix or index ‘a’ indicates absorption, ‘e’ extinction, ‘i’ dust component i , ‘p’ polarisation, ‘s’ scattering, ‘s μ ’ submicrometre-sized grains, and ‘t’ total.

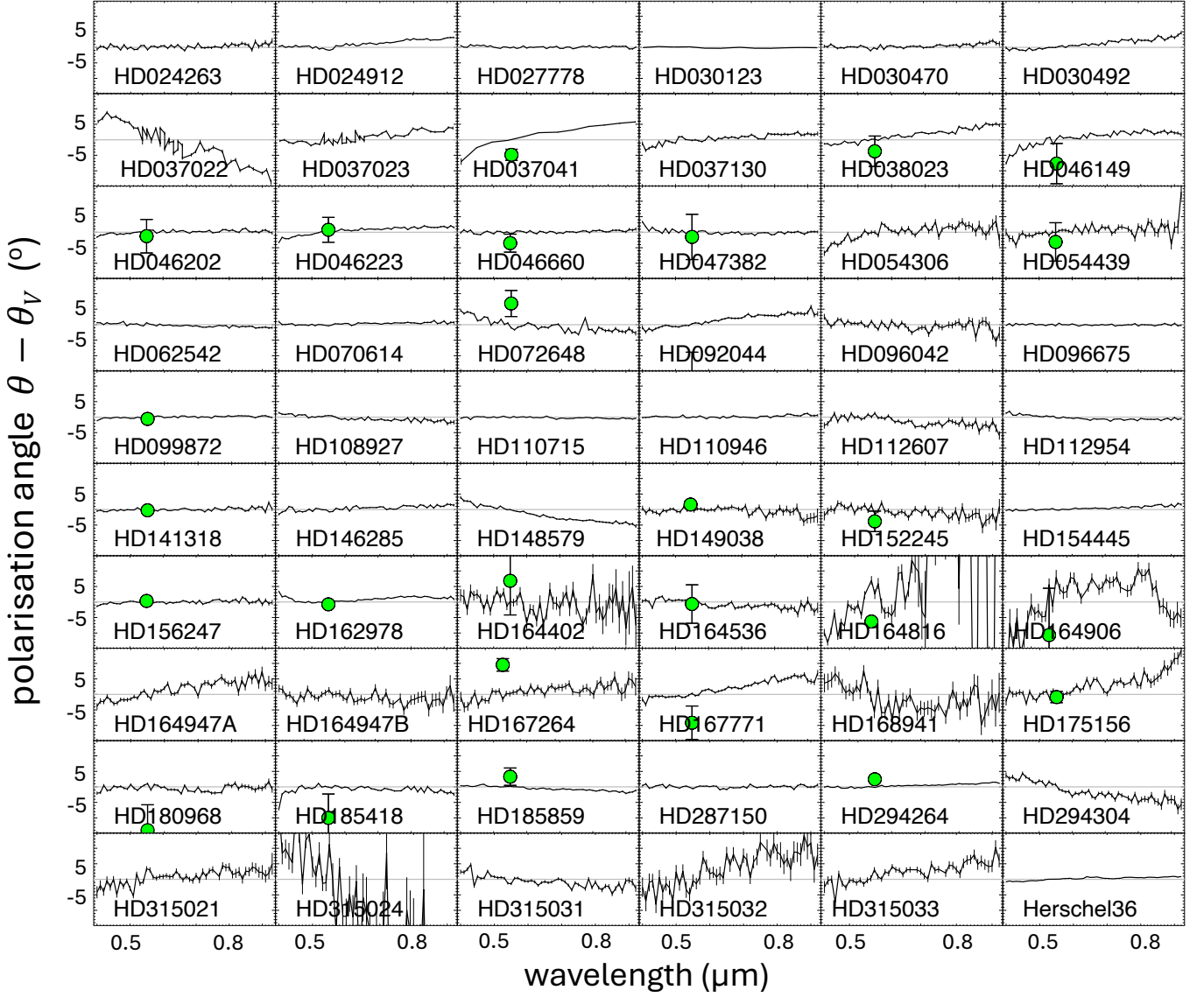


Fig. 2. The position angle of the polarisation for the 60 stars in the LIPS sample analysed in this work, offset to its value in the V optical filter, $\theta - \theta_V$ (see Table A.1). Data available in the catalogue by Heiles (2000) are shown with green circles.

3.1. Grain alignment and cross sections

$$E(\lambda - V) = \frac{2.5}{\ln 10} (\tau_\lambda - \tau_V) \quad (7)$$

and the starlight polarisation spectrum

$$p(\lambda) = N K_p(\lambda), \quad (8)$$

where $N = N^{na} + N^{su}$ (g-dust/cm²) is the total dust column density and K_p (cm²/g-dust) the total linear polarisation cross section (Eq.2).

The dust model accounts for representative solid-phase element abundances of the main absorbing dust components of the assumed grain stoichiometry and accurately explains phenomena such as wavelength-dependent reddening, starlight polarisation, and the emission of unpolarised and polarised light. It also provides the necessary grey extinction for reconciling the luminosity distances with the Gaia parallaxes (Siebenmorgen et al. 2025). We will confront it to the LIPS sample.

Various grain alignment theories, involving mechanisms such as radiative or magnetic alignment, have been proposed and were reviewed (Voshchinnikov 2012; Andersson et al. 2015). The detailed physics of grain alignment remains unresolved. In radiative alignment torque theory (Lazarian & Hoang 2007), the polarisation properties are expected to be linked to the dust temperature; however, in the diffuse ISM no such systematic effects have been observed (Planck Collaboration et al. 2020). On the other hand, (Planck Collaboration et al. 2020) examined the dispersion of polarisation angles, S , in the Milky Way as observed by Planck. This quantity is independent of dust optical properties and grain alignment efficiencies. They found that the product $S \times p$ remains approximately constant with increasing hydrogen column density, which is understood as evidence that dust polarisation is primarily driven by magnetic fields. We adopt this interpretation.

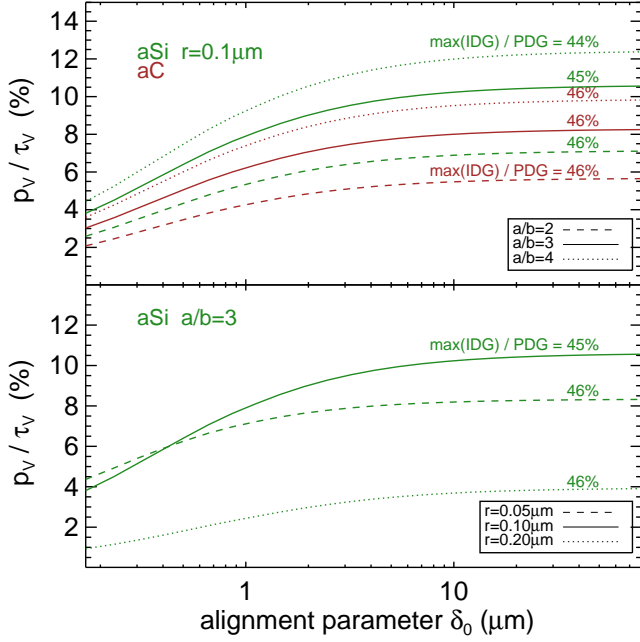


Fig. 3. Grain alignment. Polarisation efficiency in the V band as a function of the alignment parameter δ_0 for prolate grains composed of amorphous carbon (aC, brown) or silicates (aSi, green). The top panel shows variations in axial ratio for $0.1 \mu\text{m}$ grains, while the bottom panel shows variations in grain size for a fixed axial ratio $a/b = 3$. The maximum polarisation efficiency ratios for IDG vs. PDG are indicated.

Aspherical grains align with their short axes parallel to the magnetic field B . For a spheroidal particle, the maximum dichroic polarisation occurs perpendicular to the B -vector. This dichroic polarisation peaks in the optical range and is also referred to as starlight polarisation. However, the assumption of a perfect alignment is unrealistic because the angular momentum J of the grain is not necessarily parallel to B . Consequently, the grain wobbles and rotates around its axis of greatest momentum while also precessing around the magnetic field vector. This process is known as imperfect Davis-Greenstein (IDG) alignment.

The cross sections of spinning IDG aligned spheroids change periodically. The mean extinction C_e and linear polarisation C_p cross sections of a single-sized homogeneous spheroidal particle are obtained at a given wavelength

$$C_e(\lambda) = \frac{2}{\pi} \int (Q_e^{\text{TM}} + Q_e^{\text{TE}}) r^2 f(\xi, \beta) d\varphi d\omega d\beta, \quad (9)$$

$$C_p(\lambda) = \frac{1}{\pi} \int (Q_e^{\text{TM}} - Q_e^{\text{TE}}) r^2 f(\xi, \beta) \cos(2\psi) d\varphi d\omega d\beta. \quad (10)$$

The efficiency factors $Q(\lambda, r, a/b, m, \alpha)$ depend on the wavelength λ , the grain radius r , the axial ratio a/b , the optical constants m , and the angle of incidence α (Voshchinnikov 2012). They are denoted by the suffixes TM for transverse magnetic and TE for transverse electric modes of polarisation, as defined by Bohren & Huffman (1983). Computation of the efficiency factors for large spheroids becomes difficult. They are computed using Voshchinnikov & Farafonov (1993) and custom software provided by Voshchinnikov (2004). The code converges for size parameters $x = 2\pi a/\lambda$ up to $|m - 1| x \sim 22$. At such or even larger values of x , we replace the extinction cross section of the

spheroids with that of spheres using Mie theory and set the polarisation $Q_p(\lambda) = 0$. At $x > 22$, the extinction of spheroids agrees with that of spheres to within a few percent. Such large grains do not contribute significantly to the observed starlight polarisation in the optical. The average absorption and scattering cross sections C_a and C_s are obtained similar to Eq. 9 using Q_a and Q_s , respectively. The angles ψ , φ , ω , β and the mathematical description of magnetically aligned grains are provided by Hong & Greenberg (1980). The IDG alignment efficiency depends on the radius of the particle and the parameter δ_0 , where

$$f(\xi, \beta) = \frac{\xi \sin \beta}{(\xi^2 \cos^2 \beta + \sin^2 \beta)^{3/2}}, \quad (11)$$

and

$$\xi^2 = \frac{r + 0.1 \delta_0}{r + \delta_0}. \quad (12)$$

The angle between the direction of the magnetic field B and the direction of propagation k of the photons is denoted by Ω . The polarisation cross-section is zero at $\Omega = 0^\circ$ and maximum at $\Omega = 90^\circ$. At magnetic field orientations where polarisation becomes significant, the polarisation cross-section follows $C_p(\Omega) \sim \sin^2(\Omega)$, while the extinction cross-section C_e weakly depends on Ω , cf. Eqs. 20 – 21 by Draine & Fraisse (2009). Their ratio, and hence the polarisation, can be approximated by

$$\frac{p(\Omega)}{\sin^2(\Omega)} \approx \frac{p(60^\circ)}{\sin^2(60^\circ)}. \quad (13)$$

The approximation, when compared to detailed computations using Eqs. 9 – 10, is accurate within a few percent for $\Omega > 30^\circ$.

Draine & Fraisse (2009) introduced an alignment function f , where $f = 0$ represents random orientation and $f = 1$ corresponds to perfect alignment. In their models, where only silicate grains are aligned, $f \sim 1$. When considering the alignment of both silicates and carbonaceous grains, the alignment decreases, depending on the assumed grain elongation, to $f \sim 0.3$. The dust alignment efficiency are found to be similar in emission and in extinction (Planck Collaboration et al. 2014). The alignment function is strongly size-dependent: it reaches $f = 0$ at $r \lesssim 50 \text{ nm}$, rapidly increases to its maximum value at $r_p^- \sim 100 \text{ nm}$, and remains constant for larger grains (Draine & Fraisse 2009). A similar size dependence of the alignment efficiency is found for the sightlines analyzed in LIPS II (Siebenmorgen et al. 2018). Assuming IDG alignment, the FORS polarisation spectra are well reproduced when only large particles, at $r \gtrsim r_p^-$, are aligned, while smaller particles remain unaligned.

The polarisation efficiency p_V/τ_V in the V band at optical depth τ_V , as a function of the alignment parameter δ_0 , is shown in Fig. 3 for prolate grains composed of amorphous carbon (aC) or silicates (aSi) with various radii r and axial ratios a/b . In IDG alignment, the polarisation efficiency asymptotically approaches a maximum at $\delta_0 \gtrsim 10 \mu\text{m}$, where it reaches approximately 46% of the value expected in perfect Davis-Greenstein alignment (PDG).

3.2. Infrared emission per gram of dust

The total emissivity $\epsilon_i(r)$ per gram of dust for a grain of population i and particle radius r is determined from the energy balance between emission and absorption of photons from the mean intensity $J^{\text{ISRF}} \lambda$ of the ISRF (Mathis et al. 1983).

$$\int K_{a,i}(\lambda, r) J^{\text{ISRF}}(\lambda) d\lambda = \int K_{a,i}(\lambda, r) P(r, T) B(\lambda, T) dT d\lambda, \quad (14)$$

where $\epsilon_i(r)$ is given by the right-hand side, $B(\lambda, T)$ is the Planck function, and $P(r, T)$ is the temperature distribution function, which gives the probability of finding a particle of material i and radius r at temperature T (Guhathakurta & Draine 1989; Krügel 2008). This function is evaluated using an iterative scheme by Siebenmorgen et al. (1992). The quantum heating of the dust, and thus $P(T)$, needs to be evaluated only for nanoparticles, as $P(T)$ approaches a δ -function for the larger amorphous and submicrometre-sized grains. The total emission is given as the sum of the emission from all dust components.

The polarised emission $\epsilon_{i,p}$ of population i is computed by integrating over the minimum alignment radius, $r_{i,p}^-$, to the maximum radius r_i^+ :

$$\epsilon_{i,p}(\lambda, r) = \int_{r_{i,p}^-}^{r_i^+} K_{i,p}(\lambda, r) B(\lambda, T) dr, \quad (15)$$

where $K_{i,p}$ is given by Eq. 2. The polarisation cross section becomes $C_p = 0$ at a magnetic field orientation of $\Omega = 0^\circ$, for spheroids with radii below the minimum alignment radius $r_{i,p}^-$, as well as for spherical or non-aligned grains. The total polarised dust emission is the sum of the polarised emission from all components contributing to the polarisation, which include the amorphous and submicrometre-sized grains. The corresponding fractional polarisation from dust emission is

$$p = \frac{\epsilon_p}{\epsilon}. \quad (16)$$

3.3. Infrared emission per H - atoms

More material along a given sightline will increase both $E(B-V)$ and N_H . Observationally, it is assumed that the reddening scales approximately linearly with the dust column density and, if well mixed, also with the hydrogen column density such that $N_H/E(B-V)$ remains roughly constant. Bohlin et al. (1978) derived $N_H/E(B-V) = 5.8$, with this and subsequent values given in 10^{21} H-atoms $\text{cm}^{-2} \text{mag}^{-1}$, which is close to 5.9 for translucent clouds (Rachford et al. 2009). However, significantly lower values, e.g., 4.9 (Diplas & Savage 1994), as well as larger values of 7.5 (Ensor et al. 2017) and 9.4 (Nguyen et al. 2018) have been reported as well as $N_{HI}/E(B-V) = 8.3$ (Liszt 2014) and 8.8 by Lenz et al. (2017). These differences are consistent with systematic variations in the gas-to-dust mass ratio, with lower values in the Galactic plane and higher values at high Galactic latitudes.

The total dust mass, M_{dust} , is estimated by summing all atoms depleted from the gas phase and scaling by the molecular weights corresponding to the assumed grain stoichiometry. The gas mass, $M_{\text{gas}} \sim 1.4 M_H$, is calculated by summing the contributions of helium and hydrogen, assuming a He:H ratio of 1:10. At high Galactic latitudes, the derived gas-to-dust mass ratio is $M_{\text{gas}}/M_{\text{dust}} \sim 125$ (Hensley & Draine 2021; Siebenmorgen 2023). This ratio may vary by up to $\sim 50\%$ while still being consistent with elemental depletion. However, because we use relative dust abundances in our dust model, such variations, if applied to all components (Eq. 3), do not affect the fit to the reddening curves.

The gas-to-dust mass ratio and the hydrogen column density are used to scale the dust emission in the model ϵ (Eq. 14) in erg $\text{s}^{-1} \text{Hz}^{-1} \text{sr}^{-1}$ per g-dust to the Planck surface brightness I_p (erg $\text{s}^{-1} \text{Hz}^{-1} \text{sr}^{-1} \text{cm}^{-2}$ per H-atom) at 353 GHz, with atomic mass unit m_u

$$N_H = \frac{1}{m_u} \frac{M_{\text{gas}}}{M_{\text{dust}}} \frac{I_p}{\epsilon}. \quad (17)$$

For our nominal dust composition (Sect. 4.1), we find that the $N_H/E(B-V)$ ratio is 6.3 for HD 027778, 7.6 for HD 108927, and 7.3 for HD 287150, in units of 10^{21} H-atoms $\text{cm}^{-2} \text{mag}^{-1}$. These values align with the reference values and fall within the uncertainty range of the gas-to-dust mass ratio $M_{\text{gas}}/M_{\text{dust}}$.

3.4. Dust Model Fitting Procedure

The dust model is applied to sightlines with available high-quality far-ultraviolet selected reddening curves and visual extinction values derived from accurate Gaia distance estimates (A_V , Eq. 20), FORS starlight polarisation spectra, and Planck polarised emission. Best-fit dust parameters are derived using a three-step iterative procedure.

Initially, the reddening curve is fitted using the publicly available χ^2 minimization tool *absredgaia* (Siebenmorgen 2025). This tool returns the χ_r^2 of the best fit to the reddening curve and the seven model parameters: the exponent of the size distribution (q) and the relative mass fractions of the different dust components m_{vgr} , m_{vSi} , m_{PAH} , m_{aC} , m_{aSi} , m_{su} . These relative dust masses are linked to the element abundances (Eq. 3). The tool adheres to the depletion limits set by Eq. 4. Dust parameters of the general field of the ISM (Siebenmorgen 2023) are chosen as starting parameters, with an upper radius $r_{\text{su}}^+ = 3 \mu\text{m}$.

In the second step, the starlight polarisation spectrum is fitted by varying the minimum alignment radii of the amorphous grains $r_{\text{p,aC}}^-$ and $r_{\text{p,aSi}}^-$, and the magnetic field orientation Ω . The model grid of the grain radii is set to increase by 5% from one bin to the next. The dust model is run for 40×40 pairs $r_{\text{p,i}}^-$ of $i \in \{\text{aC, aSi}\}$ between 50 and 250 nm, and for each, the maximum polarisation $p(60^\circ)$ is computed. Then, Ω is varied so that, by utilizing Eq. 13, the model polarisation $p(\Omega)$ matches, if possible, the maximum of the Serkowski fit p_V (col.15 of Table A.1). The polarisation curves of the models, $p(\Omega, \lambda)$, which fit p_V , are compared to the FORS polarisation spectrum, and their χ_p^2 values are computed. Outliers in the model sample are rejected using a robust 3σ clipping based on the median absolute deviation. The three fitting parameters ($r_{\text{p,aC}}^-$, $r_{\text{p,aSi}}^-$, and Ω) are then derived from the residual distribution of models that yield the minimum χ_p^2 .

Planck Collaboration et al. (2020) introduced two criteria for constraining dust models by examining the ratio of submillimetre-to-optical polarisation. These are: the ratio of the fractional polarisation at $850 \mu\text{m}$ to the optical polarisation efficiency, defined as

$$R_{S/V} = p_{850}/(p_V/\tau_V), \quad (18)$$

and the ratio of the polarised emission intensity $P_{850} = p_{850} I_{850}$ (MJy/sr) to the optical polarisation,

$$R_{P/p} = P_{850}/p_V. \quad (19)$$

In the third step, the best-fit parameters from step 2 are retained, and the upper grain radius is varied within the range $0.25 < r_{su}^+ \leq 3 \mu\text{m}$. This results in 50 models for which the Planck-to-FORS polarisation ratios $R_{S/V}$ and $R_{P/P}$, along with their corresponding goodness-of-fit parameters χ_r^2 , χ_p^2 , $\chi_{R_{S/V}}^2$, and $\chi_{R_{P/P}}^2$, are computed. These χ^2 values are normalized to its respective median. A total goodness-of-fit parameter is then derived by assigning equal weight to the reddening curve, the FORS polarisation spectrum, and the Planck ratios: $\chi_t^2 = (\chi_r^2 + \chi_p^2 + \chi_{R_{S/V}}^2 + \chi_{R_{P/P}}^2)/4$. The upper radius of the submicrometre grains r_{su}^+ corresponds to the minimum of $\chi_t^2(r_{su}^+)$.

The polarised emission spectrum is shown for three sightlines in Fig. 4. At $850 \mu\text{m}$, the polarisation is dominated by the submicrometre particles. By increasing the radius r_{su}^+ , these grains become cooler, and their polarisation spectrum shifts to longer wavelengths so that the polarised intensity P_{850} increases as long as one remains in the Rayleigh part of that spectrum of the submicrometre grains. On the other hand, by decreasing r_{su}^+ , the submicrometre grains approach temperatures of the amorphous components, causing the polarisation spectra of both components to merge.

In the optical range the submicrometre dust component provides a grey (constant) reddening and has a marginal impact on the best-fitting model parameters, whereas in the near-infrared, the reddening is for sightlines with significant amount (m_{su}) of submicrometre grains strongly impacted by r_{su}^+ . Therefore, varying r_{su}^+ will change the fitting parameters of the reddening curve, necessitating repetition of the procedure. Fortunately, in the three steps, the dependencies on the free model parameters are weak and converge after one to two iterations. The FORS and Planck data are fitted without considering polarisation by nanoparticles.

4. Grain structure and alignment efficiency

Observations of dust polarisation in both absorption and emission provide complementary, in theory orthogonal, perspectives on dust grains, allowing constraints to be placed on their shapes, porosity, and alignment efficiencies.

4.1. Pristine sightlines

Pristine sightlines from the LIPS sample were chosen for dust modeling applications. A high-quality sample of far-UV selected reddening curves was derived by Siebenmorgen et al. (2023). Stars with multiple bright objects in the IUE (Valencic et al. 2004; Fitzpatrick & Massa 2007) and FUSE (Gordon et al. 2009) apertures were excluded. Only stars for which the spectral type and luminosity class, as derived from UVES high-resolution spectroscopy, confirm those used in the reddening estimation were retained. Furthermore, the photometric variability of stars in the high-quality sample, both in the V and G -bands, and in the $B - V$ color, was restricted to ≤ 0.03 mag.

The visual extinction A_V (Table A.1) was derived following Siebenmorgen et al. (2025) by inserting the absolute magnitude M_V and Gaia distance estimates D_{Gaia} into the photometric equation:

$$A_V = V - M_V - 5 \log D_{\text{Gaia}} + 5. \quad (20)$$

The absolute magnitude M_V was extracted from the catalogues of Bowen et al. (2008) and Wegner (2006) for the spectral type

and luminosity class provided by Siebenmorgen et al. (2023). The distances were estimated using Data Release 3 (DR3) by Gaia Collaboration et al. (2023). To ensure a reliable astrometric solution, only stars with a renormalized unit weight error (RUWE) below 1.2 were included (Luri et al. 2018). Additionally, the G -magnitude-dependent parallax error $\sigma(\pi, G)$ was computed following Maíz Apellániz (2022), and only stars with a parallax precision of $\pi/\sigma(\pi, G) > 10$ were considered. The simple inverse of the DR3 catalog parallax typically agrees with D_{Gaia} within 2%. Since parallactic distances inherently depend on priors, we verified that our distance estimate D_{Gaia} aligns with other probabilistic distance estimates within 1–2% (Bailer-Jones et al. 2021). Three stars exhibiting H -band extinction greater than their visual extinction A_V (Eq. 20) were removed from the subsample, as their luminosity distance is smaller than the trigonometric distance. This selection results in a highly accurate LIPS subsample of 27 sightlines that are ready for dust modeling.

Extinction probes the ISM in the foreground of the star, while emission traces the entire sightline. Planck Collaboration et al. (2015) established selection criteria for sightlines in order to obtain polarisation measurements of the same dust grains at different wavelengths. For this purpose, the visual extinction derived from the star's reddening must be comparable to the visual extinction estimated from the Planck maps. This criterion excludes sightlines with significant dust emission originating from material located behind the star. The limited $40'$ resolution of the Planck polarisation maps prevents a direct comparison with starlight polarisation measurements of individual stars at low Galactic latitudes. However, at Galactic latitudes $|b| \gtrsim 15^\circ$, three stars HD 027778, HD 108927, and HD 287150, exhibit significant starlight and Planck polarisation with comparable extinction values, $A_V^{850} \sim A_V$ (Table A.1). In addition, these stars show the expected reversal in polarisation angle between the polarised emission and the starlight polarisation, consistent with a difference of $90^\circ \pm 10^\circ$.

4.2. Fiducial test cases

The three stars, HD 027778, HD 108927, and HD 287150, selected in Sect. 4.1 serve as fiducial test cases. To investigate the structure of the grains, we varied the axial ratio of the prolates, $a/b \in \{1.5, 2, 2.5, 3, 4\}$, and adjusted the porosity, defined as the vacuum volume fraction, of the amorphous carbon and silicates of $V_a \in \{0, 5, 10, 20, 30, 40, 50\}$ (%) and that of the submicrometre-sized grains of $V_{su} \in \{5, 10, 20\}$ (%). We compute the volume ratios of silicate (V_{Si}), carbon (V_{C}), and vacuum (V_{su} , i.e., porosity) in the fluffy submicrometre-sized composite grains to match an abundance ratio of $[\text{Si}]/[\text{C}] \sim 3.6$ (Hensley & Draine 2021). For the three porosity levels considered in submicrometre grains, their cross-sections are computed using volume ratios $V_{\text{Si}}:V_{\text{C}}:V_{\text{su}}$ of 57:38:5, 53:37:10, and 48:32:20 (%). For the study of alignment efficiency, we examined the PDG and the IDG alignment by setting $\delta_0 \in \{0.2, 1, 10\}$ (μm) in Eq. 12. Within this sparsely sampled parameter space, we computed the dust cross-sections (Eqs. 9 – 10) over 280 frequencies and 130 radii, ranging from 6 nm to $3 \mu\text{m}$, for each of the prolate particles. In these models, a specific set of structure parameters of the particles a/b , V_a , V_{su} and alignment efficiency, was applied uniformly across all grain types and the fitting procedure described in Sect. 3.4 was used². For each star, fits to the reddening curve,

² Custom software available at:

<https://github.com/tvannieu/JISMO>

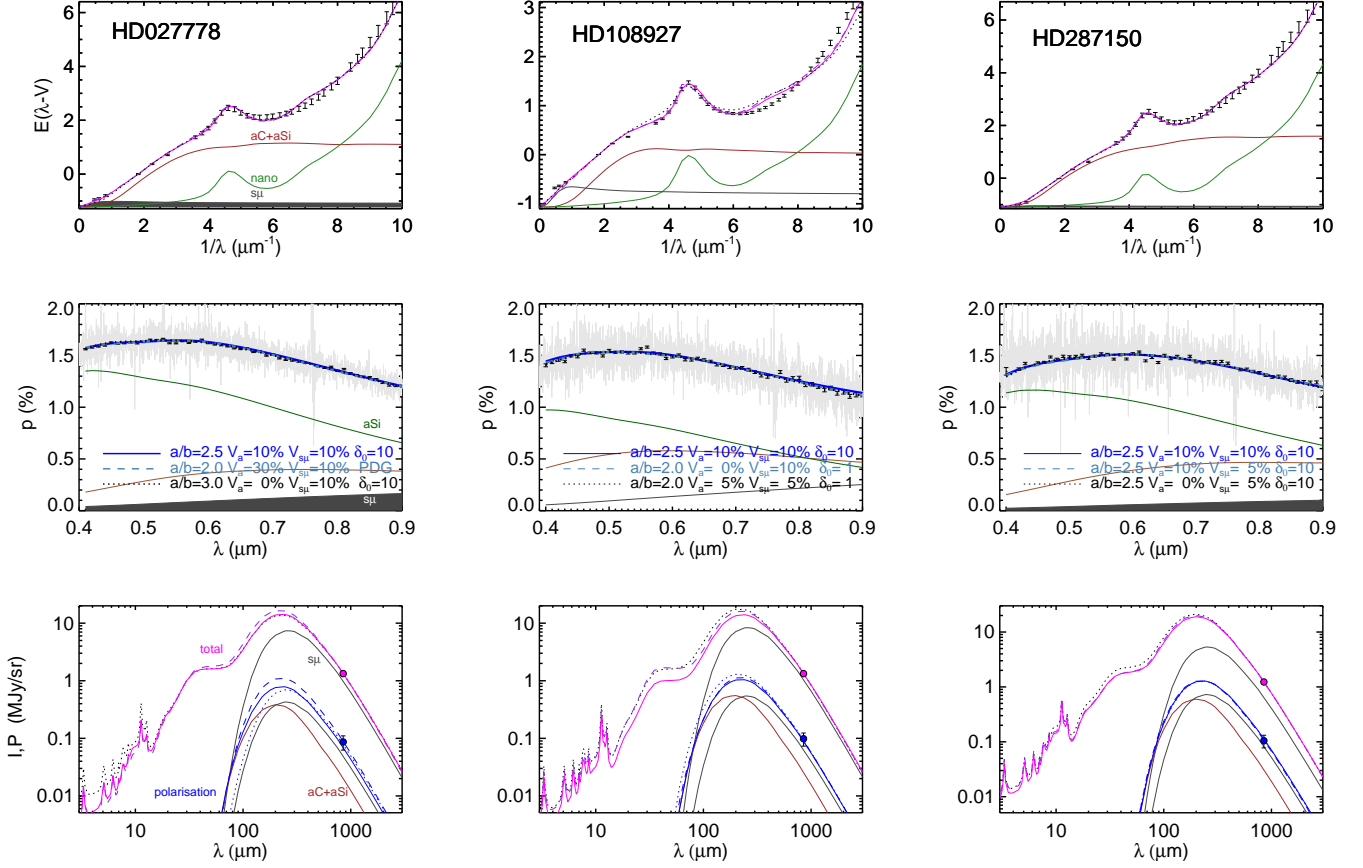


Fig. 4. Dust models for HD 027778 (left), HD 108927 (middle), and HD 287150 (right). For each star, we show the reddening curve (top), the FORS polarisation spectrum (middle), and the total (I , magenta) and polarised (P , blue) emission spectrum (bottom). The two best-fitting models (dotted and dashed lines), with parameters as annotated, are shown along with the nominal model ($a/b = 2.5$, $V_a = V_{s\mu} = 10\%$, $\delta_0 = 10\mu\text{m}$; solid lines). The dust emission is consistent with Planck 353 GHz data (filled circles). The FORS polarisation spectrum is shown as grey lines; open circles indicate the same data rebinned to a spectral resolution of $\lambda/\Delta\lambda \sim 50$. The contribution to the reddening from nanoparticles (green), amorphous grains (brown), and submicrometre-sized grains (grey) are provided and the same color scheme is used for the polarised emission spectrum. For the total emission spectrum, we show the contribution from the submicrometre-sized (grey) grains. The contribution to the FORS polarisation spectrum, from amorphous silicates (aSi, green), from amorphous carbon (aC, brown) and submicrometre-sized grains (grey) is given.

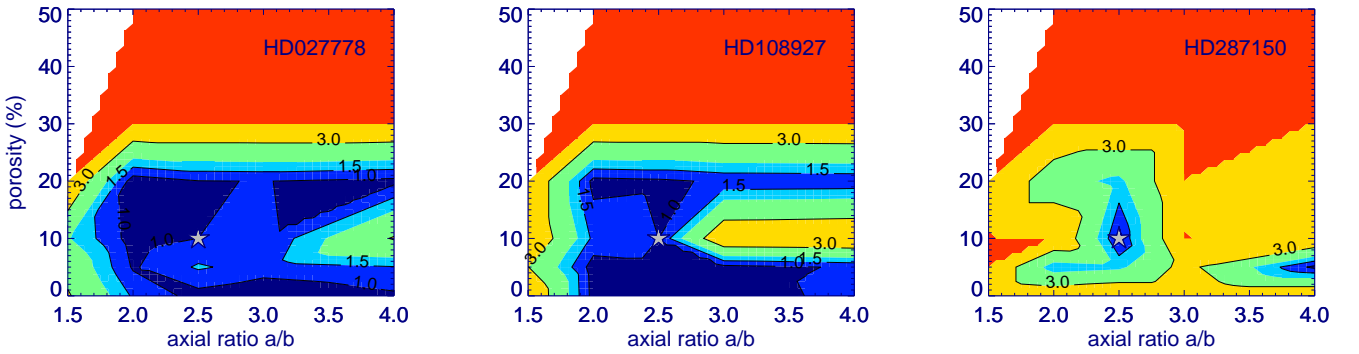


Fig. 5. The total goodness-of-fit χ^2_t , normalized to the nominal model (grey symbol), as a function of axial ratio a/b and porosity of the amorphous grains, for models with $V_{s\mu} = 10\%$ and alignment efficiency $\delta_0 = 10\mu\text{m}$, for HD 027778 (left), HD 108927 (middle), and HD 28715 (right). Regions with successful fits at $\chi^2_t \lesssim 1.5$ are shown in blue and at $\chi^2_t \gtrsim 4$ in red.

which respect element depletion constraints (Eq. 4) and incorporate the Gaia distance estimates (Eq. 20), the FORS polarisation spectrum, and the total and polarised dust emission spectrum are presented in Fig. 4. The parameter set of the cross sec-

tions with $a/b = 2.5$, $V_a = V_{s\mu} = 10\%$, and $\delta_0 = 10\mu\text{m}$ was adopted as the nominal model of the grain structure and alignment efficiency. In addition, for each star, two other models are shown that fit at similar quality as the nominal model.

There are significant degeneracies in the model grid of particle structures, where multiple models fit all datasets with comparable quality. This is visualized in Fig. 5 for models with a porosity of the submicrometre grains of $V_{su} = 10\%$ and an IDG alignment efficiency of $\delta_0 = 10\mu\text{m}$. The plots show the total goodness-of-fit, χ^2_t , normalized to the nominal model. The contour levels at $\chi^2_t = 1, 1.5$, and 3 indicate regions of similar fit quality across the axial ratio a/b and porosity V_a of the amorphous grains. The lowest contours, highlighted in blue, correspond to models with performance comparable to that of the nominal model (Fig. 5). These models typically have grain porosities $V_a \lesssim 20\%$ and axial ratios $a/b \gtrsim 2$.

For each star, a total of 250 models were computed. We find 18 models for HD 027778, 17 for HD 108927, and 3 for HD 287150 that reproduce the data with similar accuracy to the respective nominal model. Among this total of 38 models, 11 are in the PDG, 16 in IDG with $\delta_0 = 10\mu\text{m}$, 11 with $\delta_0 = 1\mu\text{m}$, and none with $\delta_0 = 0.2\mu\text{m}$. Most (75%) of the acceptable models have an axial ratio of $a/b = 2$ or 2.5. Half of the good models (those with $\chi^2_t \lesssim 1$) have amorphous grain porosities below $V_a \lesssim 5\%$, while only four such models have high porosity ($V_a > 20\%$), and none with $V_a = 50\%$. The porosity of the submicrometre grains among the acceptable models is approximately evenly distributed between $V_{su} = 5\%$ and 10%, with only one model found at $V_{su} = 20\%$. Acceptable fits are generally obtained for models with high grain alignment efficiency, axial ratios around $a/b \sim 2$, and amorphous grain porosities $V_a \lesssim 20\%$.

Most notably, only the nominal model provides a consistently high-quality fit to all datasets across the three stars. This uniqueness motivates its use for fitting the remaining stars in our sample. For this model of the grain structure and alignment efficiency, the upper radius of the submicrometre grains is $r_{su}^+ = 1.22, 0.96$ and 1.01 (μm) for HD 027778, HD 108927, and HD 287150, respectively; with other model parameters listed in Table A.2.

4.3. Dust modelling of individual sightlines

The dust model is applied to the remaining 24 sightlines selected in Sect. 4.1, for which polarised emission data from the same grains responsible for the optical polarisation are not available. These stars are located at $|b| < 15^\circ$, where the Planck observations suffer from low ($40'$) spatial resolution. The expected 90° flip in the polarisation angle between dichroic polarisation and polarised emission is also not observed (Table A.1).

The reddening curves and starlight polarisation spectra are fit using Step 1 and Step 2 of the fitting procedure (Sect. 3.4)³. The dust cross-sections of the nominal model ($a/b = 2.5$, $V_a = V_{su} = 10\%$, $\delta_0 = 10\mu\text{m}$) are applied. The model fits and the contributions of the different grain components to the reddening and polarisation spectra are shown in Fig. 6 and Fig. 7, respectively. Notable is the variation in the relative mass of the submicrometre-sized grains, typically $m_{su} = 54 \pm 21\%$ (col. 2 in Table A.2), and their contribution to the reddening curves in Fig. 6. For sightlines with a significant amount of submicrometre-sized grains, these dominate the near-infrared reddening and produce grey (constant) extinction in the optical range. The amorphous grains produce a linear rise in extinction in the optical and add grey extinction in the far-UV. The nanopar-

ticles are responsible for the 2175\AA extinction bump and the steep rise in reddening in the far-UV.

The model fits the FORS polarisation spectra generally within 1σ of the data rebinned to $\lambda/\Delta\lambda \sim 50$. The spectra follow the shape of the Serkowski formula, with noticeable deviations for HD 093222 and HD 315024; the latter star is close to the detection limit. For these two sightlines, the polarisation rises from $0.7\mu\text{m}$ toward the infrared. The former star is a multiple-cloud sightline and shows a maximum polarisation at $\lambda_{\text{max}} = 0.43\mu\text{m}$ and a large gradient in the polarisation angle with wavelength of $d\theta/d\lambda = 97^\circ/\mu\text{m}$ (Table A.1). In a single-cloud scenario with grains aligned by the same magnetic field, it is expected that the polarisation angle remains constant and that the polarisation peaks close to $\lambda_{\text{max}} = 0.55\mu\text{m}$. Indeed, Mandarakas et al. (2024) fit the observed wavelength dependence of the polarisation angle towards HD 093222 using a two-cloud scenario. In our sample, there are two more multiple-cloud sightlines, HD 037903 and HD 152245, that show significant variation in the polarisation angle, with $d\theta/d\lambda = 5.3$ and $6.8^\circ/\mu\text{m}$, and maximum polarisations at $\lambda_{\text{max}} = 0.66$ and $0.62\mu\text{m}$, respectively. There are also five single-cloud sightlines⁴, which show variations of $6.6 \lesssim d\theta/d\lambda$ ($^\circ/\mu\text{m}$) $\lesssim 18.5$, while the other sightlines show a weak wavelength dependence of the polarisation angle, with $d\theta/d\lambda < 5^\circ/\mu\text{m}$.

The Serkowski fit is generally thought to trace the typical size of aligned grains in a single absorbing cloud. This is a simplified interpretation, because the polarisation is the sum of the contributions from different dust components—most importantly, amorphous carbon and silicate grains—which peak at different wavelengths and may arise from different dust clouds along the sightline Mandarakas et al. (2024). The dichroic polarisation is dominated by the amorphous dust component, with silicate grains contributing predominantly at shorter wavelengths than carbon particles, e.g. HD 112607 in Fig. 7. The minimum grain alignment radii for both grain types vary and are typically $r_p^- \sim 0.1\mu\text{m}$ (cols. 9 and 10 in Table A.2). The contribution of submicrometre-sized grains to the polarisation is marginal in the optical but increases toward longer wavelengths, reaching a level of $\sim 0.3\%$ towards HD 092044 (Fig. 7).

The dust model parameters of the 27 sightlines are given in Table A.2. The relative masses m_{vgr} , m_{vSi} , m_{PAH} , m_{aC} , m_{aSi} , and m_{su} in 1 g of dust (%) for the individual dust components are listed in cols. 2–7. The exponent of the dust size distribution q , the minimum alignment radii of amorphous silicate and carbon grains $r_{p,\text{Si}}^-$ and $r_{p,\text{aC}}^-$, and the derived magnetic field orientation Ω are given in cols. 8–11. Other derived parameters include the total Si and C abundances in dust relative to H (in ppm; cols. 12–13), and the percentage contribution of the submicrometre-sized grains to the total extinction in the optical (col. 14). The median and 1σ scatter of each parameter are provided at the bottom of Table A.2, indicating substantial variation across individual sightlines. Typically, about half of the dust mass resides in submicrometre-sized grains, which contribute roughly one-third of the total extinction. The dust abundances of $[\text{Si}]/[\text{H}] \sim 38$ and $[\text{C}]/[\text{H}] \sim 100$ (ppm) in the model agree with estimates for the diffuse ISM by Hensley & Draine (2021).

5. Conclusion

We completed the Large Interstellar Polarisation Survey (LIPS), which obtained FORS spectropolarimetry in the $0.38\text{--}0.92\mu\text{m}$ wavelength range for 161 sightlines through the diffuse ISM.

³ Custom software available at:
<https://github.com/tvannieu/JISM>

⁴ HD 054439, HD 046223, HD 092044, HD 038023, and HD 294304

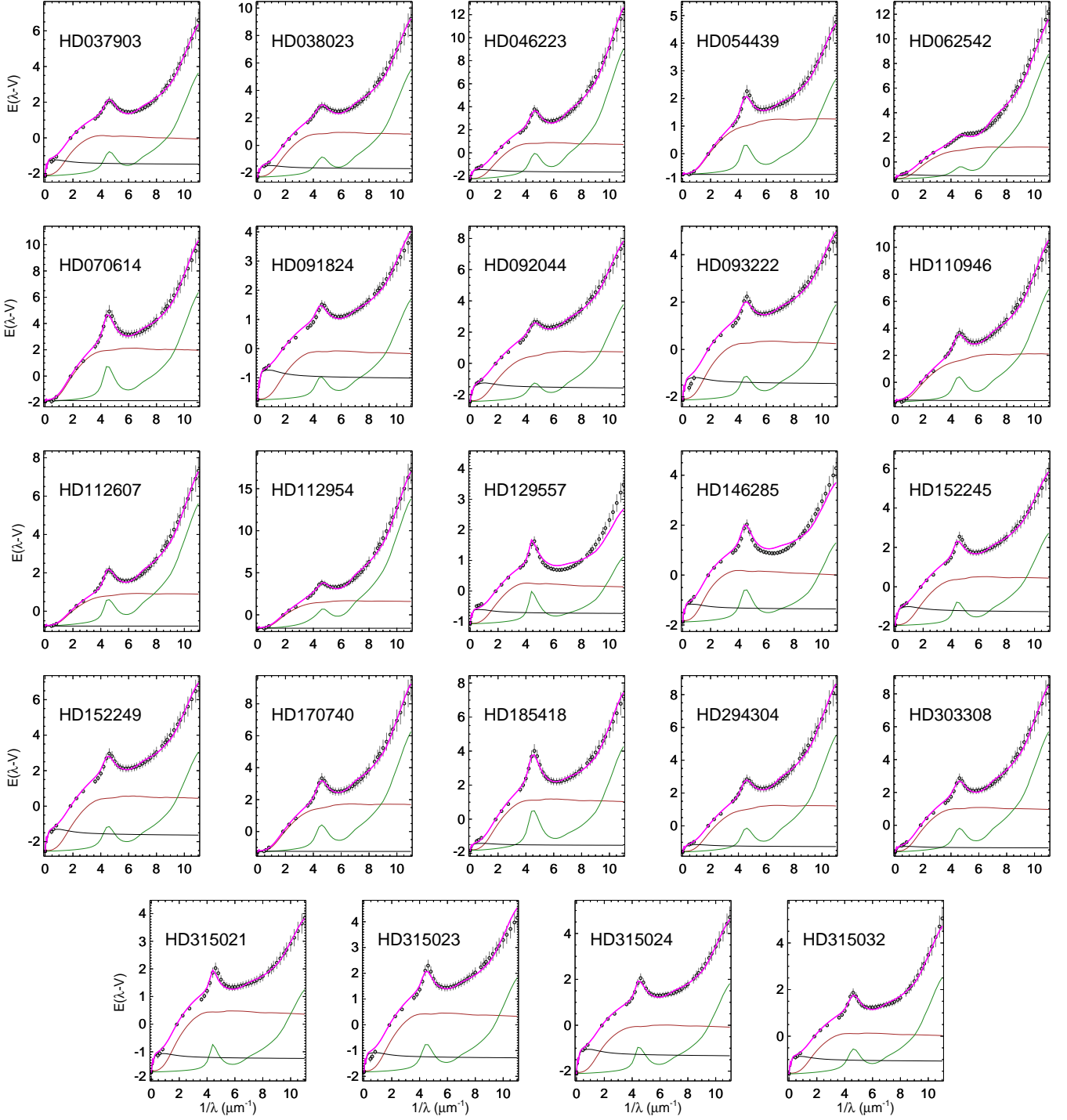


Fig. 6. Dust model fits to the absolute reddening curves $E(\lambda - V)$ of 24 sightlines. Data points (circles) cover the range $0.09 - 2.2 \mu\text{m}$ and are complemented at infinite wavelengths by $-A_V$ (Table A.1). The best fit with contributions from the nano-grains (green), the amorphous carbon and silicates (brown), and submicrometre-sized grains (dark), are shown, with model parameters listed in Table A.2. Notable is the dominance of the submicrometre-sized grains in the infrared and their wavelength-independent contribution to the optical/far UV, respectively.

Sixty polarisation spectra were presented in this work. The LIPS sample was selected based on the availability of reddening curves: in the far-UV from the IUE and FUSE satellite missions, in the optical from ground-based photometry, and in the near-infrared from 2MASS. High-resolution spectra were obtained with UVES/VLT to verify the spectral types and luminosity classes of the stars used for deriving the reddening curves and

to probe the number of clouds along individual sightlines. Gaia parallaxes were used to estimate the visual extinction A_V necessary for reconciling the derived luminosity distances with the trigonometric distance estimates for the same stars. The dichroic polarisation spectra were complemented by Planck $850 \mu\text{m}$ polarimetry.

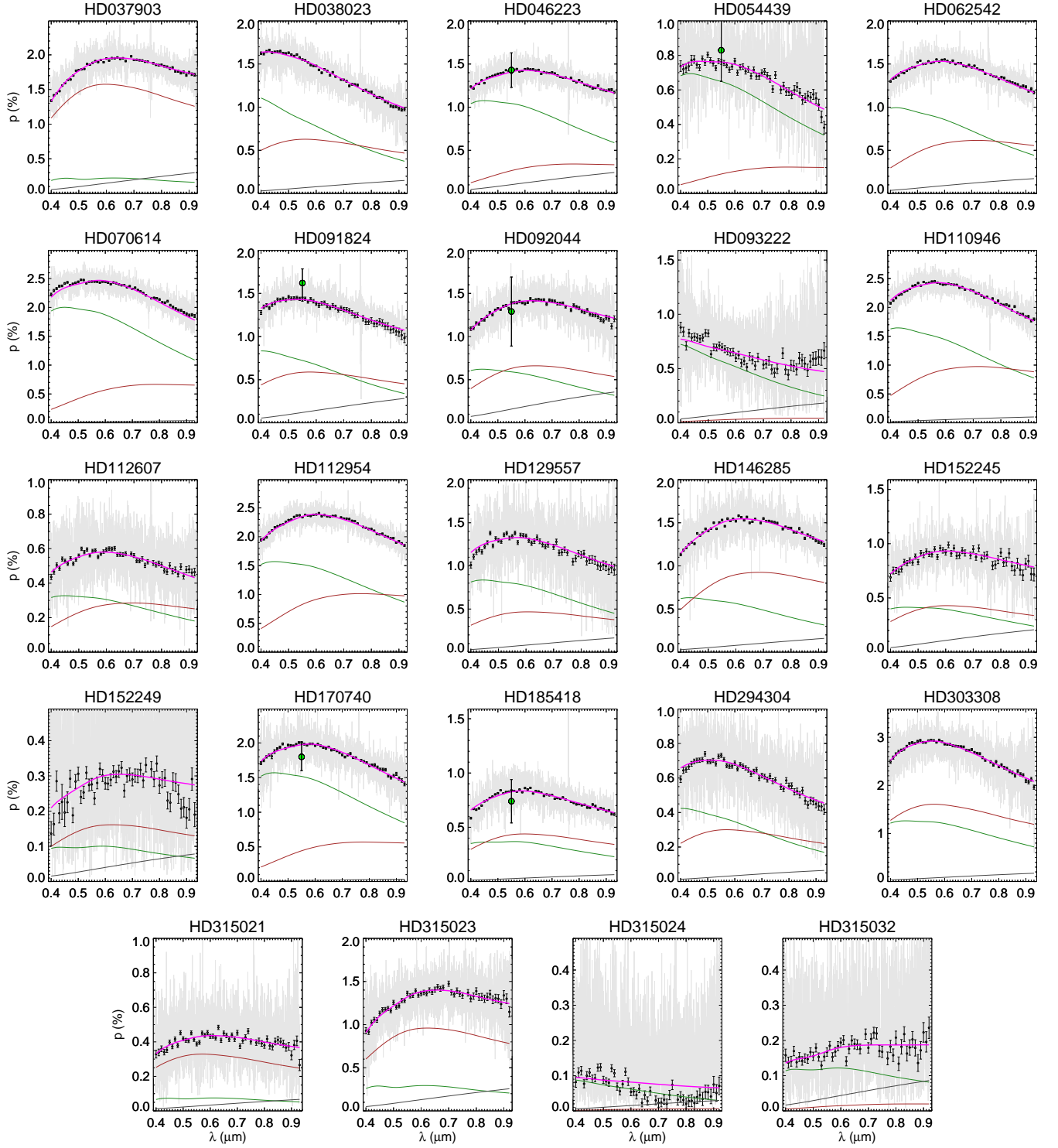


Fig. 7. FORS polarisation spectra, shown both with the original unbinned data (grey lines), and after rebinning then at spectral resolution $\lambda/\Delta\lambda \sim 50$ (black open circles). The error bars associated to the rebinned spectra refer to 1σ . In each panel, the magenta line represents the dust model fit, while the remaining lines show the contributions due to the amorphous silicates (green line), the amorphous carbon and (brown line), and submicrometre-sized grains (black line). Data available in the stellar polarisation catalogue by Heiles (2000) are shown with a green circle.

This dataset is used to constrain the properties of grains in the diffuse ISM using a three-component model that includes nanoparticles, amorphous grains, and submicrometre-sized grains. The nanoparticles are responsible for the far-UV rise in the reddening curve, the 2175 Å bump, and the mid-infrared emission bands. The amorphous grains produce grey

(constant) extinction in the far-UV, an almost linear decline toward longer wavelengths, and the far IR emission. The submicrometre grains contribute grey extinction in the optical, a linear decline in the near-IR, and the submillimetre emission. The optical polarisation is dominated by amorphous grains, while the 850 μm polarisation is dominated by the submicrometre grains.

Within the sample, three sightlines exhibit both significant starlight and Planck polarisation, with comparable extinction values, $A_V^{850} \sim A_V$, and the expected 90° reversal in the polarisation angle between polarised emission and starlight polarisation. The polarisation data for these sightlines provide an almost orthogonal perspective on the aligned grains, enabling constraints on their particle shape, porosity, and alignment efficiency. Although degeneracies exist among the dust model parameters, a good fit to all three sightlines is obtained using a high grain alignment efficiency of $\delta_0 = 10\mu\text{m}$ of grains larger than $\sim 0.1\mu\text{m}$, an axial ratio $a/b = 2.5$, and porosities of 10% for both the amorphous and submicrometre grains. This nominal model is applied to 24 additional sightlines that have high-quality reddening curves and dichroic polarisation spectra but ambiguous Planck polarisation due to high background contamination. A single-cloud model for these sightlines generally provides a fit consistent with the 1σ uncertainty.

The contribution of submicrometre grains is most evident in the near-infrared extinction and, with few exceptions, is marginal in the FORS spectropolarimetry. Overall, we find that submicrometre grains are responsible for approximately one-third of the total extinction and comprise about half of the total dust mass. Significant variations in dust abundances persist from cloud to cloud.

The present analysis is limited by the low spatial resolution of the Planck maps, which leads to source confusion. A follow-up submillimetre survey with a high spatial resolution polarimeter is required whenever it becomes available to combine polarised emission and starlight polarisation measurements through the diffuse ISM.

Acknowledgements. This research has made use of the services of the ESO Science Archive Facility and the SIMBAD database operated at CDS, Strasbourg, France (Wanger et al. 2000) and partially based on observations collected at the European Southern Observatory under ESO programmes Observations collected at the European Southern Observatory are based under ESO programmes: 60.A-9036(A) and 70.D-0191(A).

References

Andersson, B.-G., Lazarian, A., & Vaillancourt, J. E. 2015, *Annual Review of Astronomy and Astrophysics*, 53, 501
 Appenzeller, I., Fricke, K., Fürst, W., et al. 1998, *The Messenger*, 94, 1
 Bagnulo, S., Cox, N. L. J., Cikota, A., et al. 2017, *A&A*, 608, A146
 Bailer-Jones, C. A. L., Rybizki, J., Founesneau, M., Demleitner, M., & Andrae, R. 2021, *AJ*, 161, 147
 Bianchi, S. 2024, *A&A*, 691, A330
 Blasberger, A., Behar, E., Perets, H. B., Brosch, N., & Tielens, A. G. G. M. 2017, *ApJ*, 836, 173
 Bohlin, R. C., Savage, B. D., & Drake, J. F. 1978, *ApJ*, 224, 132
 Bohren, C. F. & Huffman, D. R. 1983, *Absorption and scattering of light by small particles*, Research supported by the University of Arizona and Institute of Occupational and Environmental Health. New York, Wiley-Interscience, 1983, 541 p.
 Bowen, D. V., Jenkins, E. B., Tripp, T. M., et al. 2008, *ApJS*, 176, 59
 Chini, R., Krügel, E., Haslam, C. G. T., et al. 1993, *A&A*, 272, L5
 Chini, R., Krügel, E., Lemke, R., & Ward-Thompson, D. 1995, *A&A*, 295, 317
 Cutri, R. M., Skrutskie, M. F., van Dyk, S., et al. 2003, *2MASS All Sky Catalog of point sources*. (ADS)
 Dekker, H., D’Odorico, S., Kaufer, A., Delabre, B., & Kotzlowski, H. 2000, in *Society of Photo-Optical Instrumentation Engineers (SPIE) Conference Series*, Vol. 4008, *Optical and IR Telescope Instrumentation and Detectors*, ed. M. Iye & A. F. Moorwood, 534–545
 Demyk, K., Gromov, V., Meny, C., et al. 2022, *A&A*, 666, A192
 Diplas, A. & Savage, B. D. 1994, *ApJ*, 427, 274
 Draine, B. T. 2003, *ApJ*, 598, 1017
 Draine, B. T. & Faisse, A. A. 2009, *ApJ*, 696, 1
 Draine, B. T. & Hensley, B. S. 2021, *ApJ*, 909, 94
 Ensor, T., Cami, J., Bhatt, N. H., & Soddu, A. 2017, *ApJ*, 836, 162
 Fitzpatrick, E. L. & Massa, D. 2007, *ApJ*, 663, 320

Gaia Collaboration, Vallenari, A., Brown, A. G. A., et al. 2023, *A&A*, 674, A1
 Galametz, M., Madden, S., Galliano, F., et al. 2009, *A&A*, 508, 645
 Galliano, F., Madden, S. C., Jones, A. P., Wilson, C. D., & Bernard, J. P. 2005, *A&A*, 434, 867
 Gordon, K. D., Cartledge, S., & Clayton, G. C. 2009, *ApJ*, 705, 1320
 Guhathakurta, P. & Draine, B. T. 1989, *ApJ*, 345, 230
 Guillet, V., Fanciullo, L., Verstraete, L., et al. 2018, *A&A*, 610, A16
 Heiles, C. 2000, *AJ*, 119, 923
 Hensley, B. S. & Draine, B. T. 2021, *ApJ*, 906, 73
 Hong, S. S. & Greenberg, J. M. 1980, *A&A*, 88, 194
 Kennicutt, R. C., Calzetti, D., Aniano, G., et al. 2011, *PASP*, 123, 1347
 Kim, S.-H. & Martin, P. G. 1995, *ApJ*, 444, 293
 Krügel, E. 2008, *An introduction to the physics of interstellar dust (IOP)*
 Krügel, E. & Siebenmorgen, R. 1994, *A&A*, 288, 929
 Krügel, E., Siebenmorgen, R., Zota, V., & Chini, R. 1998, *A&A*, 331, L9
 Krüger, H., Strub, P., Grün, E., & Sterken, V. J. 2015, *ApJ*, 812, 139
 Landgraf, M., Baggaley, W. J., Grün, E., Krüger, H., & Linkert, G. 2000, *J. Geophys. Res.*, 105, 10343
 Lazarian, A. & Hoang, T. 2007, *MNRAS*, 378, 910
 Lenz, D., Hensley, B. S., & Doré, O. 2017, *ApJ*, 846, 38
 Liszt, H. 2014, *ApJ*, 780, 10
 Luri, X., Brown, A. G. A., Sarro, L. M., et al. 2018, *A&A*, 616, A9
 Madden, S. C., Rémy-Ruyer, A., Galametz, M., et al. 2013, *PASP*, 125, 600
 Maíz Apellániz, J. 2022, *A&A*, 657, A130
 Mandarakas, N., Tassis, K., & Skaliadis, R. 2024, *3D ISM structure challenges the Serkowski relation*
 Mathis, J. S., Mezger, P. G., & Panagia, N. 1983, *A&A*, 128, 212
 Mathis, J. S., Rimpl, W., & Nordsieck, K. H. 1977, *ApJ*, 217, 425
 Nguyen, H., Dawson, J. R., Miville-Deschênes, M. A., et al. 2018, *ApJ*, 862, 49
 Ormel, C. W., Min, M., Tielens, A. G. G. M., Dominik, C., & Paszun, D. 2011, *A&A*, 532, A43
 Planck Collaboration, Abergel, A., Ade, P. A. R., et al. 2014, *A&A*, 566, A55
 Planck Collaboration, Ade, P. A. R., Aghanim, N., et al. 2015, *A&A*, 576, A106
 Planck Collaboration, Aghanim, N., Akrami, Y., et al. 2020, *A&A*, 641, A12
 Popovic, B., Wiseman, P., Sullivan, M., et al. 2024, *MNRAS*, 534, 2263
 Rachford, B. L., Snow, T. P., Destree, J. D., et al. 2009, *ApJS*, 180, 125
 Rémy-Ruyer, A., Madden, S. C., Galliano, F., et al. 2013, *A&A*, 557, A95
 Serkowski, K., Mathewson, D. S., & Ford, V. L. 1975, *ApJ*, 196, 261
 Siebenmorgen, R. 2023, *A&A*, 670, A115
 Siebenmorgen, R. 2025, *Dark_dust: Visual extinction estimator A_V using submicrometer-sized grains*
 Siebenmorgen, R., Heymann, F., & Chini, R. 2025, *ApJ*, 979, L45
 Siebenmorgen, R., Krelowski, J., Smoker, J., Galazutdinov, G., & Bagnulo, S. 2020, *A&A*, 641, A35
 Siebenmorgen, R., Kruegel, E., & Mathis, J. S. 1992, *A&A*, 266, 501
 Siebenmorgen, R., Krügel, E., & Chini, R. 1999, *A&A*, 351, 495
 Siebenmorgen, R., Smoker, J., Krelowski, J., Gordon, K., & Chini, R. 2023, *A&A*, 676, A132
 Siebenmorgen, R., Voshchinnikov, N. V., & Bagnulo, S. 2014, *A&A*, 561, A82
 Siebenmorgen, R., Voshchinnikov, N. V., Bagnulo, S., et al. 2018, *A&A*, 611, A5
 Smoker, J., Haddad, N., Iwert, O., et al. 2009, *The Messenger*, 138, 8
 Stecher, T. P. & Donn, B. 1965, *ApJ*, 142, 1681
 Vaillancourt, J. E., Andersson, B. G., Clemens, D. P., et al. 2020, *ApJ*, 905, 157
 Valencic, L. A., Clayton, G. C., & Gordon, K. D. 2004, *ApJ*, 616, 912
 Voshchinnikov, N. V. 2004, *Astrophys. Space Phys. Res.*, 12, 1
 Voshchinnikov, N. V. 2012, *J. Quant. Spec. Radiat. Transf.*, 113, 2334
 Voshchinnikov, N. V. & Farafonov, V. G. 1993, *Ap&SS*, 204, 19
 Wang, S., Li, A., & Jiang, B. W. 2015a, *MNRAS*, 454, 569
 Wang, S., Li, A., & Jiang, B. W. 2015b, *ApJ*, 811, 38
 Wegner, W. 2006, *MNRAS*, 371, 185
 Westphal, A. J., Stroud, R. M., Bechtel, H. A., et al. 2014, *Science*, 345, 786
 Ysard, N., Jones, A. P., Guillet, V., et al. 2024, *A&A*, 684, A34
 Zubko, V. G., Mennella, V., Colangeli, L., & Bussolletti, E. 1996, *MNRAS*, 282, 1321

Appendix A: Tables and continued Figure 1

Table A.1. Stars with derived Planck, reddening, FORS and Serkowski parameters. The meaning of the columns is explained in Sect. 2.

1	2	3	4	5	6	7	8	9	10	11	12	13	14	15	16	17
Star		PLANCK				Reddening				FORS				Serkowski		
Name	$ b $	I_{850} MJy/sr	P_{850} %	θ_{850} °	A_V^{850} mag	A_V mag	A_V^{ref} mag	Ref	SM	Date	p_V %	θ_V °	$d\theta/d\lambda$ °/ μm	p_{max} %	λ_{max} μm	k_p
HD 024263	35	1.00	6.0± 2.4	77± 18	0.8	–	0.7	V	S	2019-02-24	1.1 ± 0.1	149 ± 0.5	2 ± 0.7	1.08	0.58	1.04
HD 024912	13	1.28	6.9± 1.8	27± 6	1.1	–	1.0	V	M	2015-12-25	1.4 ± 0.1	111 ± 0.6	7 ± 1.1	1.43	0.62	1.16
“	“	“	“	“	“	“	“	“	“	2018-11-17	“	“	“	“	“	“
HD 027778	17	1.33	6.5± 1.8	152± 7	1.2	1.2	1.1	G	M	2015-12-23	1.6 ± 0.1	69 ± 0.3	-1 ± 0.3	1.65	0.52	1.08
“	“	“	“	“	“	“	“	“	“	2018-11-14	“	“	“	“	“	“
HD 030123	17	1.96	6.8± 1.2	179± 4	1.6	–	1.6	F	M	2020-10-02	2.8 ± 0.1	85 ± 0.2	-1 ± 0.2	2.76	0.54	1.14
HD 030470	21	1.26	6.5± 2.2	178± 12	1.1	–	1.1	F	S	2019-03-17	1.4 ± 0.1	76 ± 0.5	2 ± 0.6	1.36	0.56	1.20
HD 030492	21	1.26	6.7± 2.2	171± 4	1.1	–	1.2	F	S	2019-03-18	1.4 ± 0.1	77 ± 0.4	9 ± 1.5	1.37	0.59	1.16
HD 037022	19	353	2.9± 0.0	40± 16	294	–	1.9	F	S	2015-12-23	0.2 ± 0.1	146 ± 2.9	-52 ± 5.7	0.27	0.77	1.25
“	“	“	“	“	“	“	“	“	“	2020-10-02	“	“	“	“	“	“
HD 037023	19	353	2.9± 0.0	40± 68	294	–	1.7	V	S	2015-12-23	0.5 ± 0.1	61 ± 1.3	13 ± 1.7	0.51	0.71	0.82
“	“	“	“	“	“	“	“	“	“	2020-10-01	“	“	“	“	“	“
HD 037041	19	255	2.7± 0.0	40± 29	212	–	1.1	V	S	2020-10-25	0.8 ± 0.1	101 ± 0.7	20 ± 3.6	0.94	0.72	1.45
HD 037130	19	5.34	7.4± 0.4	30± 17	4.5	–	1.3	F	S	2019-03-18	1.2 ± 0.1	138 ± 0.7	7 ± 1.4	1.35	0.74	1.17
HD 037367	1	4.46	4.7± 0.5	70± 35	3.7	–	1.5	V	M	B17	1.0 ± 0.1	15 ± 0.9	0 ± 1.2	1.02	0.63	1.13
HD 037903	17	35.4	2.2± 0.1	65± 34	30	–	1.5	G	M	2015-12-25	1.9 ± 0.1	121 ± 0.3	5 ± 0.9	1.96	0.66	1.42
“	“	“	“	“	“	“	“	“	“	2018-11-12	“	“	“	“	“	“
HD 038023	19	11.7	3.8± 0.2	20± 23	9.7	2.3	1.6	F	S	2019-02-23	1.6 ± 0.1	87 ± 0.7	13 ± 2.1	1.64	0.43	0.93
“	“	“	“	“	“	“	“	“	“	2019-03-18	“	“	“	“	“	“
HD 046149	2	4.89	4.6± 0.4	65± 30	4.1	–	1.3	F	M	2018-12-07	0.6 ± 0.1	5 ± 1.0	13 ± 2.4	0.64	0.64	1.17
HD 046202	2	4.85	4.2± 0.4	62± 26	4.0	–	1.5	G	M	2018-12-08	1.0 ± 0.1	178 ± 0.5	2 ± 0.5	1.00	0.60	1.05
HD 046223	2	6.26	4.2± 0.3	64± 14	5.2	2.3	1.5	V	S	2018-12-07	1.4 ± 0.1	168 ± 0.6	8 ± 1.2	1.43	0.59	1.05
HD 046660	1	3.75	5.6± 0.6	87± 19	3.1	–	1.7	F	M	2020-10-02	1.8 ± 0.1	17 ± 0.3	1 ± 0.4	1.81	0.60	1.09
HD 047382	1	3.76	5.8± 0.5	69± 5	3.1	–	1.4	F	M	2018-12-11	0.9 ± 0.1	155 ± 0.6	-2 ± 0.8	0.95	0.65	1.28
“	“	“	“	“	“	“	“	“	“	2018-12-14	“	“	“	“	“	“
HD 054306	2	3.39	3.4± 0.6	56± 2	2.8	–	0.6	F	M	2019-02-23	0.5 ± 0.1	147 ± 1.5	12 ± 2.3	0.47	0.55	0.98
HD 054439	2	3.07	3.3± 0.6	56± 7	2.6	0.7	0.8	F	S	2015-12-23	0.8 ± 0.1	139 ± 0.6	7 ± 2.3	0.77	0.51	1.17
HD 062542	9	3.17	0.3± 0.4	147± 31	2.6	1.4	1.2	G	S	2018-12-07	1.5 ± 0.1	26 ± 0.3	-3 ± 0.5	1.53	0.58	1.21
HD 070614	3	5.87	2.2± 0.3	32± 65	4.9	–	2.1	F	M	2019-02-06	2.4 ± 0.1	58 ± 0.2	2 ± 0.4	2.47	0.54	1.01
HD 072648	2	7.38	0.1± 0.2	57± 36	6.1	–	1.2	F	M	2019-02-24	0.7 ± 0.1	3 ± 0.9	-11 ± 2.0	0.74	0.56	1.03
“	“	“	“	“	“	“	“	“	“	2019-03-17	“	“	“	“	“	“
HD 073882	1	10.8	1.7± 0.2	72± 2	9.0	–	2.5	G	M	B17	1.9 ± 0.1	164 ± 0.5	-1 ± 0.8	2.08	0.69	1.30
HD 075309	2	5.05	2.3± 0.3	114± 31	4.2	–	0.9	F	M	B17	0.6 ± 0.1	54 ± 1.9	-7 ± 3.6	0.62	0.51	1.33
HD 079186	2	3.89	1.0± 0.4	102± 36	3.2	–	1.3	V	S	B17	2.6 ± 0.1	47 ± 0.3	-2 ± 0.5	2.61	0.52	1.19
HD 089137	4	1.14	3.1± 1.5	101± 28	0.9	–	0.7	V	S	2019-02-06	0.4 ± 0.1	39 ± 1.3	-4 ± 1.6	0.41	0.64	1.09
HD 091824	0	16.0	2.3± 0.1	20± 13	13	–	0.8	F	M	2018-12-14	1.4 ± 0.1	97 ± 0.4	4 ± 0.8	1.43	0.53	1.08
HD 091983	0	17.6	1.0± 0.1	74± 33	15	–	0.9	F	S	B17	1.1 ± 0.1	131 ± 1.0	18 ± 3.2	1.11	0.56	0.95
HD 092044	0	18.8	2.0± 0.1	89± 19	16	2.4	1.4	F	S	2020-10-04	1.4 ± 0.1	160 ± 0.5	12 ± 1.9	1.42	0.63	1.33
HD 093205	1	33.5	0.3± 0.0	17± 8	28	–	1.2	V	M	B17	2.1 ± 0.1	100 ± 0.4	-5 ± 1.0	2.10	0.55	1.16
HD 093222	1	22.0	0.2± 0.1	55± 11	18	–	1.8	G	M	B17	0.7 ± 0.1	134 ± 3.9	97 ± 12.2	0.77	0.43	1.45
HD 093632	1	28.5	1.0± 0.0	151± 8	24	–	2.3	V	M	B17	1.1 ± 0.1	53 ± 1.1	-20 ± 4.9	1.47	0.84	1.29
HD 094493	1	11.6	0.3± 0.1	146± 51	9.7	–	0.8	V	M	B17	0.6 ± 0.1	107 ± 2.2	12 ± 4.5	0.67	0.43	1.04
HD 096042	1	7.68	1.8± 0.2	97± 73	6.4	–	0.9	V	M	2015-01-02	0.6 ± 0.1	115 ± 0.9	-4 ± 1.5	0.61	0.52	0.85
HD 096675	15	1.76	10.6± 0.8	19± 21	1.5	–	1.0	G	S	2019-03-14	3.2 ± 0.1	130 ± 0.2	0 ± 0.2	3.19	0.55	1.20
HD 097484	1	11.0	1.2± 0.1	44± 74	9.2	–	1.5	V	M	B17	0.9 ± 0.1	60 ± 1.4	10 ± 2.2	0.96	0.52	1.18
HD 099872	11	1.28	13.9± 1.2	31± 3	1.1	–	1.1	G	M	S14	3.2 ± 0.1	118 ± 0.3	1 ± 0.3	3.27	0.58	1.27
“	“	“	“	“	“	“	“	“	“	2019-03-09	“	“	“	“	“	“
HD 103779	1	10.8	1.8± 0.1	170± 5	9.0	–	0.7	G	M	B17	0.6 ± 0.1	75 ± 1.7	-26 ± 5.2	0.62	0.52	1.76
HD 104705	0	17.0	1.2± 0.1	66± 70	14	–	1.2	F	S	B17	0.8 ± 0.2	86 ± 3.5	-7 ± 7.2	0.77	0.62	0.89
HD 108927	15	0.92	7.4± 1.9	29± 3	0.8	1.1	0.7	F	S	2019-03-09	1.5 ± 0.1	122 ± 0.4	-5 ± 0.8	1.53	0.52	1.15
HD 110715	2	5.12	5.9± 0.4	168± 3	4.3	–	1.3	F	S	2019-03-08	2.8 ± 0.1	75 ± 0.2	-1 ± 0.3	2.79	0.58	1.28
“	“	“	“	“	“	“	“	“	“	2019-03-14	“	“	“	“	“	“
HD 110946	2	5.10	5.4± 0.4	166± 3	4.3	1.5	1.6	F	S	2019-02-11	2.4 ± 0.1	79 ± 0.3	1 ± 0.4	2.43	0.56	1.30
HD 112607	1	16.7	1.5± 0.1	146± 6	14	0.7	0.8	F	S	2019-03-04	0.6 ± 0.1	63 ± 0.6	-7 ± 1.5	0.58	0.59	1.47
HD 112954	0	29.2	0.4± 0.1	41± 87	24	1.5	1.7	F	S	2019-02-24	2.3 ± 0.1	45 ± 0.3	-4 ± 0.7	2.39	0.60	1.35
HD 122879	2	8.07	2.0± 0.2	173± 13	6.7	–	1.1	V	M	B17	1.8 ± 0.1	70 ± 0.5	-5 ± 0.9	1.81	0.55	1.52
HD 129557	4	2.32	6.2± 0.9	171± 0	1.9	1.1	0.5	V	S	B17	1.3 ± 0.1	80 ± 0.7	1 ± 1.0	1.33	0.57	1.54
HD 134591	20	0.76	4.2± 3.0	131± 73	0.6	–	0.6	V	M	B17	0.3 ± 0.1	114 ± 5.4	24 ± 11.6	0.31	0.43	0.54
HD 141318	1	33.8	2.5± 0.1	149± 8	28	–	0.8	V	M	2014-10-10	2.4 ± 0.1	51 ± 0.2	1 ± 0.5	2.46	0.58	1.27
HD 146285	18	2.12	4.9± 1.2	123± 15	1.8	1.9	1.2	F	S	2019-03-19	1.5 ± 0.1	18 ± 0.5	4 ± 0.8	1.55	0.63	1.47
HD 147888	18	4.59	7.2± 0.6	132± 12	3.8	–	2.0	G	S	B17	3.3 ± 0.1	54 ± 0.2	-3 ± 0.6	3.49	0.66	1.49
HD 147889	17	17.6	1.1± 0.1	123± 37	15	–	4.3	V	S	B17	3.4 ± 0.2	177 ± 0.4	-7 ± 1.4	4.20	0.81	1.30
HD 148379	2	8.01	1.8± 0.3	132± 12	6.7	–	2.4	V	M	B17	1.9 ± 0.1	30 ± 0.6	-1 ± 0.7	1.95	0.58	0.94
HD 148579	16	3.91	2.5± 0.6	139± 30	3.3	–	1.4	F	S	2021-01-23	2.0 ± 0.1	79 ± 0.7	-15 ± 2.4	2.12	0.66	1.16
HD 149038	3	5.42	1.4± 0.4	161± 43	4.5	–	1.1	V	M	2019-04-02	1.0 ± 0.1	29 ± 0.6	-1 ± 1.2	1.02	0.57	1.47
HD 151804	2	5.95	3.0± 0.4	148± 15	5.0	–	1.3	V	M	B17	1.1 ± 0.1	43 ± 0.8	-8 ± 1.6	1.12	0.57	1.21
HD 152235	1	17.9	2.1± 0.1	138± 67	15	–	2.2	V	M	B17	0.8 ± 0.1	115 ± 1.5	-6 ± 2.7	0.79	0.47	1.54
HD 152245	2	6.15	0.7± 0.4	142± 3	5.1	–	1.1	V	M	2015-02-06	0.9 ± 0.1	49 ± 1.1	-7 ± 1.7	0.93	0.62	1.48
HD 152249	1	15.9	2.2± 0.2	144± 10	13	2.5	1.6	G	S	B17	0.3 ± 0.1	64 ± 3.9	-27 ± 6.2	0.30	0.65	2.37
HD 153919	2	5.28	1.4± 0.4	80± 20	4.4	–	2.0	V	M	B17	2.7 ± 0.1	10 ± 0.3	7 ± 1.2	2.67	0.57	1.09
HD 154445	23	1.27	16.6± 1.7	180± 1	1.1	–	1.2	F	S	2020-10-03	3.7 ± 0.1	91 ± 0.2	3 ± 0.6	3.74	0.56	1.15
HD 156247	22	0.78	15.1± 2.7	178± 1	0.7	–	0.7	F	S	2020-10-03	2.0 ± 0.1	87 ± 0.2	2 ± 0.5	2.04	0.56	1.20
HD 162978	0	40.7	2.1± 0.1	126± 36	34	–	1.2	V	M	2018-11-06	1.3 ± 0.1	-1 ± 0.3	3 ± 0.8	1.41	0.65	1.53
HD 163181	4	3.71														

Table A.1. Stars with derived reddening, FORS, Serkowski and Planck parameters. The meaning of the columns is explained in Sect. 2.

1	2	3	4	5	6	7	8	9	10	11	12	13	14	15	16	17
Star		PLANCK				Reddening				FORS				Serkowski		
Name	$ b $	I_{850} MJy/sr	p_{850} %	θ_{850} °	A_{850}^V mag	A_V mag	A_V^{ref} mag	Ref	SM	Date	p_V %	θ_V °	$d\theta/d\lambda$ °/ μm	p_{max} %	λ_{max} μm	k_p
HD 164947A	1	23.9	1.4± 0.1	111± 51	20	–	1.1	F	S	2020-10-03	0.5 ± 0.1	72 ± 1.2	17 ± 2.8	0.53	0.56	0.88
HD 164947B	1	23.8	1.4± 0.1	111± 28	20	–	1.1	F	S	2020-10-03	0.6 ± 0.1	49 ± 1.0	-5 ± 1.8	0.59	0.60	0.90
HD 167264	2	9.02	1.7± 0.2	151± 41	7.5	–	1.0	V	S	2020-10-03	0.5 ± 0.1	102 ± 1.3	11 ± 2.1	0.57	0.65	1.80
HD 167771	1	13.2	1.2± 0.2	59± 78	11	2.2	1.5	G	S	2019-02-20	0.5 ± 0.1	47 ± 0.9	16 ± 2.6	0.57	0.68	1.24
“										2019-03-19						
HD 167838	0	24.7	2.3± 0.1	122± 66	21	–	2.1	V	M	B17	0.3 ± 0.1	97 ± 2.7	48 ± 8.7	0.32	0.57	1.56
HD 168076	1	40.5	2.4± 0.1	146± 11	34	–	2.6	V	M	B17	3.4 ± 0.1	66 ± 0.3	-5 ± 0.9	3.41	0.58	1.33
HD 168941	6	1.47	0.8± 1.6	80± 60	1.2	–	1.2	G	M	2019-03-03	0.1 ± 0.1	50 ± 3.9	-18 ± 4.2	0.15	0.73	1.35
HD 169454	1	36.6	2.4± 0.1	119± 14	30	–	3.6	V	S	B17	2.1 ± 0.1	15 ± 0.8	-9 ± 1.6	2.12	0.58	1.26
HD 170740	1	25.9	2.2± 0.1	129± 38	22	–	1.4	F	M	B17	2.0 ± 0.1	77 ± 0.5	-5 ± 0.9	1.98	0.56	1.23
HD 175156	8	1.33	1.8± 1.8	80± 52	1.1	–	1.1	V	S	2020-10-03	0.5 ± 0.1	42 ± 1.1	18 ± 3.7	0.54	0.54	1.23
HD 180968	5	2.98	2.3± 0.6	30± 84	2.5	–	0.8	F	S	2019-04-08	0.5 ± 0.1	36 ± 0.7	-1 ± 0.9	0.52	0.53	1.05
HD 185418	2	4.03	2.7± 0.5	148± 34	3.4	–	1.4	G	M	2019-03-25	0.8 ± 0.1	24 ± 0.4	-1 ± 1.2	0.84	0.60	1.65
HD 185859	1	7.09	4.3± 0.3	111± 16	5.9	–	1.6	V	S	2020-10-04	2.2 ± 0.1	5 ± 0.2	-4 ± 0.7	2.27	0.50	1.25
“										2020-10-06						
HD 203532	32	1.14	7.4± 1.5	48± 12	1.0	–	0.9	F	S	2018-11-05	1.4 ± 0.1	126 ± 0.4	-1 ± 0.6	1.41	0.58	1.21
HD 210121	44	0.85	8.8± 2.3	46± 20	0.7	–	0.8	F	S	B17	1.3 ± 0.1	156 ± 1.1	9 ± 1.7	1.35	0.44	0.48
HD 287150	21	1.23	8.5± 2.2	172± 11	1.0	1.1	1.2	F	S	2019-03-19	1.5 ± 0.1	72 ± 0.3	0 ± 0.4	1.51	0.56	0.97
HD 294264	19	19.9	3.0± 0.1	13± 26	17	–	2.8	F	M	2019-03-18	2.8 ± 0.1	78 ± 0.3	3 ± 0.5	3.14	0.72	1.37
“										2019-03-19						
HD 294304	17	2.16	1.8± 0.9	68± 18	1.8	1.6	1.2	F	S	2020-10-01	0.7 ± 0.1	140 ± 1.5	-18 ± 2.8	0.70	0.52	1.47
HD 303308	1	44.0	0.6± 0.0	148± 41	37	–	1.4	V	M	B17	2.9 ± 0.1	99 ± 0.2	0 ± 0.4	2.92	0.55	1.32
HD 315021	1	25.6	1.4± 0.1	110± 36	21	1.7	1.2	F	S	2019-02-10	0.4 ± 0.1	56 ± 2.3	11 ± 2.4	0.44	0.62	1.38
HD 315023	1	25.0	0.9± 0.1	122± 61	21	1.8	1.5	F	S	B17	1.3 ± 0.1	151 ± 0.7	1 ± 0.9	1.40	0.68	1.41
HD 315024	1	28.3	1.4± 0.1	109± 16	24	2.1	1.2	F	S	2020-10-04	0.1 ± 0.1	183 ± 9.2	-130 ± 29.3	0.10	0.43	2.50
HD 315031	1	32.3	1.4± 0.1	109± 26	27	–	1.2	F	S	2020-10-04	0.6 ± 0.1	45 ± 0.8	-9 ± 1.8	0.58	0.64	0.95
HD 315032	1	41.7	1.4± 0.1	109± 48	35	1.6	1.0	F	S	2020-10-04	0.2 ± 0.1	66 ± 3.8	29 ± 5.5	0.19	0.87	0.50
HD 315033	1	41.0	1.0± 0.1	102± 83	34	–	1.4	V	S	2020-10-04	0.4 ± 0.1	95 ± 1.5	17 ± 3.1	0.41	0.64	1.65
Herschel 36	1	58.9	1.1± 0.0	91± 87	49	–	0.7	F	S	2020-10-05	6.8 ± 0.2	95 ± 0.2	3 ± 0.5	7.19	0.64	1.61
Walker 67	1	58.9	1.1± 0.0	91± 16	49	–	0.7	F	S	B17	4.1 ± 0.3	17 ± 0.6	-6 ± 1.2	5.17	0.81	1.47

Notes: B17: Bagnulo et al. (2017).

Table A.2. Dust parameters of the 27 sightlines that have been modelled. The derived C and Si abundances in the dust and the contribution of submicrometre grains to the total optical depth as well as the median and 1σ variations are provided.

1	2	3	4	5	6	7	8	9	10	11	12	13	14
Star	m_{Si}	m_{Si}	m_{VSi}	m_{aC} (%)	m_{vgr}	m_{PAH}	q	$r_{\text{p, Si}}^-$ (nm)	$r_{\text{p, aC}}^-$ (nm)	Ω (°)	$\frac{[\text{Si}]}{[\text{H}]}$ (ppm)	$\frac{[\text{C}]}{[\text{H}]}$ (ppm)	$\left(\frac{r_{\text{Si}}}{r_{\text{C}}}\right)_V$ (%)
HD 027778	24	37	27	7	4	1	2.4	130	158	49	41	79	17
HD 037903	63	16	10	8	2	1	2.0	233	66	48	46	155	37
HD 038023	56	22	13	6	2	1	2.3	47	47	29	38	92	33
HD 046223	54	21	17	4	3	1	2.2	158	183	39	45	100	32
HD 054439	–	57	22	13	5	3	2.7	143	201	45	38	90	–
HD 062542	43	20	28	6	2	1	2.6	130	136	45	54	114	23
HD 070614	25	41	18	10	4	2	2.3	158	192	54	37	93	3
HD 091824	69	17	7	5	1	1	2.2	102	57	39	42	111	52
HD 092044	61	20	11	6	1	1	2.6	150	102	34	43	115	45
HD 093222	63	18	9	8	1	1	2.3	62	245	30	32	109	40
HD 108927	30	36	21	9	3	1	2.0	97	59	45	38	93	31
HD 110946	32	32	22	9	3	2	2.7	136	136	56	38	94	9
HD 112607	–	40	40	12	6	2	2.5	158	124	33	38	89	–
HD 112954	14	29	41	10	3	3	2.5	158	166	60	45	109	1
HD 129557	63	25	5	4	2	1	2.0	150	72	50	37	90	38
HD 146285	63	18	6	10	2	1	2.0	136	112	38	28	120	33
HD 152245	62	21	10	5	1	1	2.4	166	84	30	38	93	45
HD 152249	63	21	9	5	1	1	2.3	201	92	16	38	94	44
HD 170740	22	39	25	9	4	1	2.5	158	183	64	39	87	3
HD 185418	49	30	9	7	3	2	2.2	183	76	27	35	96	20
HD 287150	16	33	33	13	3	2	2.8	150	201	69	37	96	6
HD 294304	48	25	17	7	2	1	2.6	112	69	23	38	92	26
HD 303308	46	26	18	7	2	1	2.3	166	47	55	38	93	18
HD 315021	61	22	7	8	1	1	2.2	222	51	22	34	104	35
HD 315023	61	22	8	7	1	1	2.2	222	88	44	35	101	37
HD 315024	67	15	7	8	2	1	2.3	47	245	11	45	170	46
HD 315032	64	18	10	6	2	0	2.2	201	245	24	43	130	42
median	54	22	13	7	2	1	2.3	112	112	–	38	96	32
σ	21	10	10	2	1	1	0.2	48	64	–	5	20	16

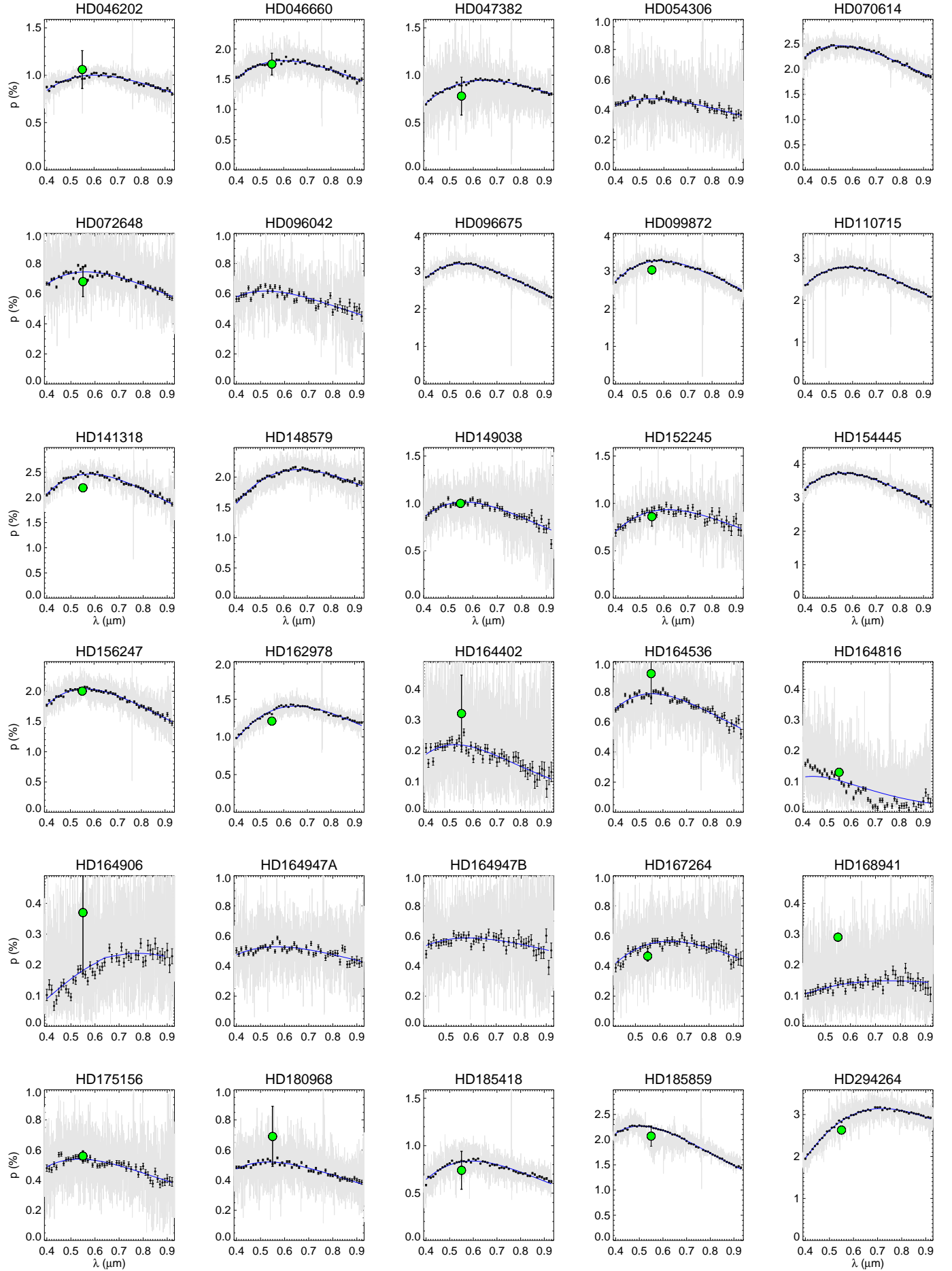


Fig. A.1. FORS polarisation spectra. – continued –

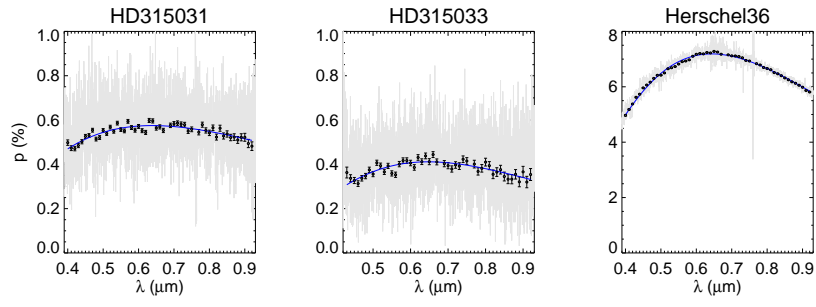


Fig. A.2. FORS polarisation spectra. – continued –